Galileo/EPD user guide

P. Kollmann[1], C. Paranicas[1], A. Lagg[2], E. Roussos[2], Z. H. Lee-Payne[3], M. Kusterer[1], D. Smith[1], N. Krupp[2], J. Vandegriff[1]

[1] Johns Hopkins University Applied Physics Laboratory, Laurel, MD, USA

[2] Max Planck Institute for Solar System Research, Göttingen, Germany

[3] Aberytwyth University, Aberystwyth, UK

Version from 2022/05/06, 10:41for v31 of the channelized data.

This guide is archived at ESSOAr, where updates may be posted.

DOI: https://doi.org/10.1002/essoar.10503620.1

For questions and comments please contact Peter.Kollmann@jhuapl.edu

Contents

1 Outline **2**
- 1.1 Mission and Instrument . . . 2
- 1.2 Data . . . 2
- 1.3 Comparison with other compilations . . . 2
- 1.4 This guide . . . 2
- 1.5 Galileo orbits . . . 2

2 Instrument description **2**
- 2.1 Subsystems . . . 3
- 2.2 Data products . . . 3
- 2.3 Available channels . . . 3
- 2.4 Best guess channels . . . 7
- 2.5 Available resolutions . . . 7
- 2.6 Calibration shield and motor step . . . 13
- 2.7 Event Data . . . 13

3 Data files content **16**
- 3.1 File types . . . 16
- 3.2 File format . . . 16
- 3.3 EPD channels low to high resolution files . . . 16
  - 3.3.1 Header . . . 16
  - 3.3.2 Radiation rates and intensities . . . 16
  - 3.3.3 Auxiliary data . . . 21
- 3.4 CMS event data . . . 22

4 Corrections to the data **22**
- 4.1 Dead time correction . . . 22
- 4.2 Background and contamination . . . 23
- 4.3 High energy electron spectra . . . 26
- 4.4 Instrument degradation mitigation . . . 28
- 4.5 Anomalous instrument performance . . . 29
- 4.6 Outstanding Issues . . . 29
  - 4.6.1 Unresolved instrument degradation . . . 29
  - 4.6.2 Mixed species channels . . . 30

5 Example data **30**
- 5.1 Radial intensity profiles . . . 30
- 5.2 Energy spectra . . . 31
- 5.3 Pitch angle distributions . . . 31
- 5.4 Event data . . . 34

6 Acknowledgements **35**

1 Outline

1.1 Mission and Instrument

The Galileo mission was the first to orbit Jupiter and lasted from 1995 to 2003. Its data set is unique even compared to contemporary data from the Juno mission since Galileo had an equatorial orbit, as it is necessary to sample equatorially mirroring particles. Galileo also had several close moon flybys. It carried instrumentation designed to provide measurements of >MeV electrons. Different to for example optical instruments that can also respond to such particles (*Davis et al.*, 2016; *Carlton et al.*, 2016; *Becker et al.*, 2017), an instrument designed to measure radiation is much more straightforward to calibrate.

Here we describe Galileo's EPD suite (Energetic Particle Detector) and its measurements. EPD measures energetic charged particles roughly in the energy range of tens of keV to tens of MeV while distinguishing particle species. (For details see Tab. 1-4 and Sec. 4.3).

1.2 Data

The data set includes the following

- Data from record mode (Sec. 2.5)
- Data from real time mode (Sec. 2.5)
- Event data (Sec. 2.7)
- Cleaned, processed, calibrated differential intensities (Sec. 3.3.2)
- Raw count rates (Sec. 3.3.2)
- Electron spectra up to 20MeV as a higher order data product (Sec. 4.3)
- Spacecraft position and instrument look direction (Sec. 3.3.3)
- Magnetic L-shells and equatorial pitch angles calculated in the Khurana magnetic field model (Sec. 3.3.3)

Data are sorted by time.

1.3 Comparison with other compilations

The original release of the data in NASA's Planetary Data Archive (PDS) (`https://pds-ppi.igpp.ucla.edu/mission/Galileo/GO/EPD`) mostly included count rates and some auxiliary data. While all record mode data was used, the real time data only included 16 of the available 48 channels. Data were sorted by moon flybys and instrument mode.

The data set described here was developed through a NASA PDART grant at JHU/APL. An earlier version of the data provided here was released to the AMDA database (`http://amda.irap.omp.eu/`, in the folder Parameters/ AMDA DataBase/ Galileo/ EPD). It might be updated with the version delivered here in the future. The delivered PDS data are version 31. As this is the first public delivery, the PDS version is 1.0. The PDS data should be identical to what is on the APL Galileo website (`http://sd-www.jhuapl.edu/Galileo_EPD/` under "Calibrated Data").

1.4 This guide

Section 2 of this document fills in gaps in the EPD documentation and summarizes information that can be found in *Williams et al.* (1992); *Hunt-Ward and Armstrong* (2003); *Mauk et al.* (2004); *Kollmann and Choo* (2019); *Kollmann et al.* (2018). We then describe the content of the newly delivered PDS data (Sec. 3) and how the data has been processed (Sec. 4). At the end we also show sample data, explain typical features and possible pitfalls (Sec. 5).

1.5 Galileo orbits

Times during the Galileo mission are sometimes roughly described with codes of letter plus number, for example E12, G8, etc. The numbers is a running orbit number, the letter is the first letter of the moon that was passed near closest approach to Jupiter. Figure 2 associates orbit numbers with dates.

2 Instrument description

This section explains what is measured by EPD. For a quick overview over the EPD channels, jump to Tab. 1.

2.1 Subsystems

EPD includes the LEMMS (Low-Energy Magnetospheric Measurements System) and CMS (Composition Measurement System) instruments (*Williams et al.*, 1992). Schematics of the mechanical structure and main components are shown in Fig. 1. Both LEMMS and CMS are double-ended and have a low energy and high energy telescope (LET and HET, respectively). LEMMS/LET uses solid state detectors (SSDs) and a magnetic deflection to separate electrons, LEMMS/HET uses solid state detectors only. For SSD-only systems, identification of particles relies on how much energy was or was not deposited in individual detectors. CMS/LET is sometimes also referred to as CMS/TOFxE because it measures ion time-of-flight (TOF) and deposited energy (E), a combination that allows to distinguish ion species. CMS/HET consists of the two apertures CMS/DeltaExE/A and B. Both apertures use SSDs and differ in their geometry factor. In order to minimize the likelihood of interpreting instrumental artifacts as physical signatures, it is important to understand the details of the measurement techniques. Details about this topic can be found throughout this guide and otherwise in *Williams et al.* (1992).

2.2 Data products

EPD has two main data products: Channelized data (Sec. 2.3) and event data (Sec. 2.7). We provide both data products. For most purposes, only the channelized data is important. Unless stated otherwise, all descriptions in this guide, particularly on the corrections to the data (Sec. 4), are about the channelized data.

2.3 Available channels

The EPD instrument bins counted particles into "coincidence channels" that cover various ranges of particle energy and mass. The coincidence channels use signals from several SSDs and/or TOF-information in coincidence (triggering several detectors at the same time) or anticoincidence (triggering one but not another detector). "Singles channels" keep track of the total raw count rates of the SSDs or Start and Stop signals of the TOF system.

Example figures based on channelized data can be found in Sec. 5.

We provide a compilation of the energy ranges and geometry factors for all native Galileo/EPD channels in Tab. 1 and 2. Artificially created channels provided in this data set are listed in Tab. 3 and will be explained further in Sec. 4.3 and 4.4.

The upper and lower energies provided for the channels in the tables are usually their "nominal" energy passbands as provided earlier (*Williams et al.*, 1992; *Lagg*, 1998; *Mauk et al.*, 2004). The center energies provided here are calculated as the logarithmic average of the passband boundaries, which is a standard approach. The center energy (sometimes also called mean energy) of a channel is ideally chosen as the energy where the fully resolved energy dependent intensity spectrum (if it were known with certainty) would equal the intensity averaged over the passband that is measured by the respective channel (*Selesnick and Blake*, 2000). This criterion is exactly fulfilled for the center energies used here if the energy spectrum is a power law with exponents of $\gamma = 0$ or $\gamma = -2$.

The provided geometry factors of the channels only allow for an exact conversion from raw count rates to calibrated intensities if the particle intensity spectra are constant in energy. This is a common approximation, even though it is usually not exactly true. The resulting error is smaller if the energy range of the channel is smaller. Avoiding this approximation requires the use of the full response functions (geometry factor as a continuous function of energy) instead of a single-value geometry factor. References on where to find values for these functions are provided in the comment column of the tables. All response functions have been published in peer-reviewed journals with the exception of the response functions of the E and F channel that we reproduce in Fig. 3. Full response functions need to be used in order to derive reliable differential intensity values from channels with very wide energy ranges.

For the DC channels, the lower passbands are defined here as the energy where the geometry factor (*Jun et al.*, 2002) rises above 50% of its maximum. The geometry factor for these channels is the average value above this threshold. The response of these channels rises quickly with energy. Lowering the response threshold to 10% of the maximum geometry factor does not change the lower passband significantly. The B1 channel on the other has a response that slowly rises with energy and therefore has no well-defined lower passband. The energy passbands and geometry factors provided for these channels are different from what have been published before. Irrespective of the precise value, it is important to know that these numbers are only useful for zeroth order estimates of the intensity spectra. It is important to remember that channels usually also have a small, but non-zero responsiveness outside of the passbands. There are circumstances, for example when the intensity

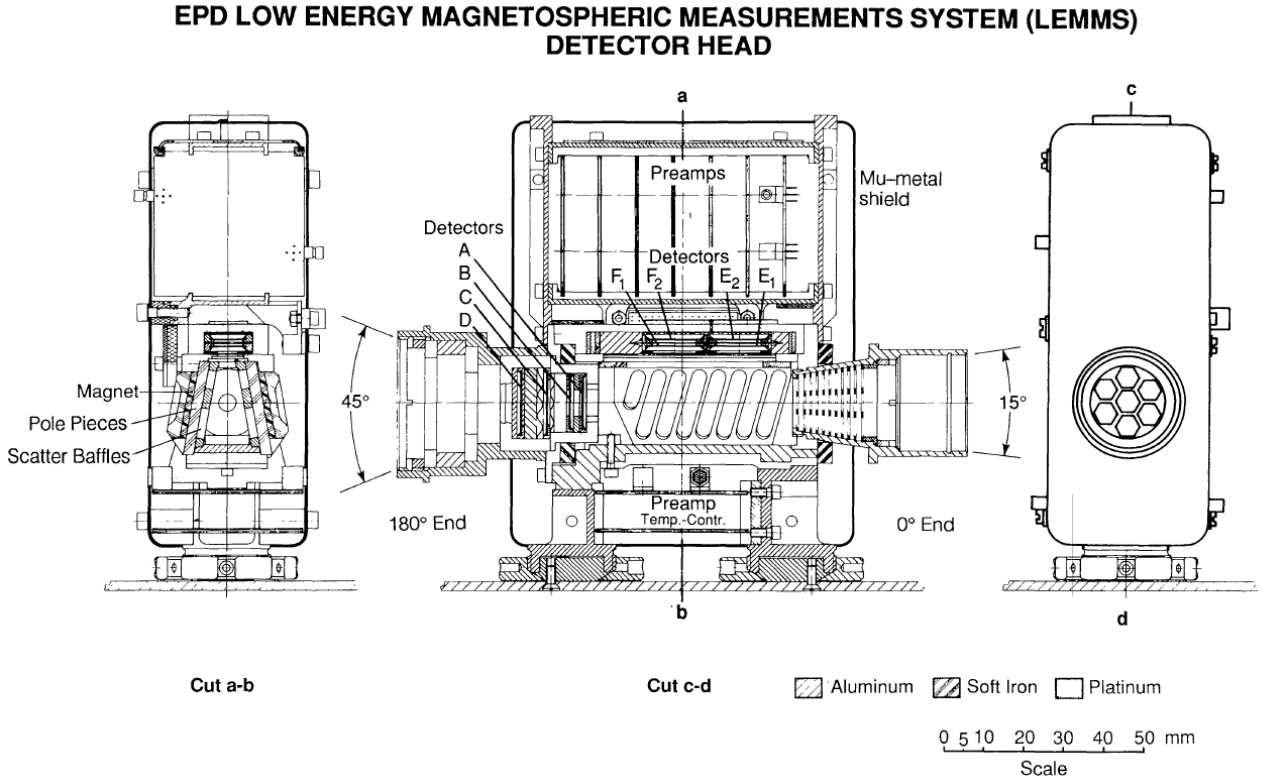

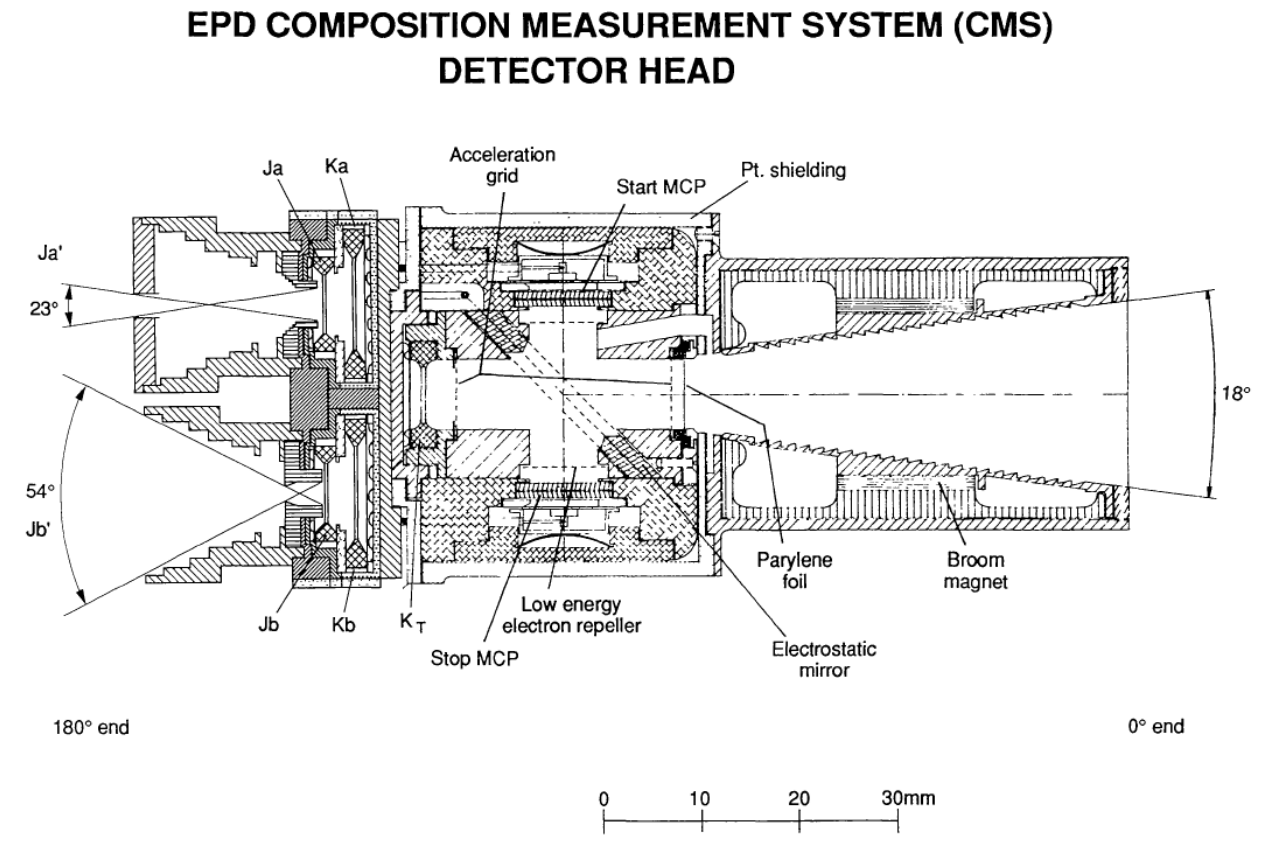

Figure 1: Schematics of the LEMMS (upper panel) and CMS (lower panel) subsystems of EPD. Components labeled as A, F_1, Ja, etc. are names and locations of solid state detectors. Figure from *Williams et al.* (1992).

Orbit Number	Periapsis Date	Periapsis DOY	Periapsis Range [RJ]	Moon closest approach	Apoapsis Date
J0	1995-12-07	341	4.00	1995-12-07	1996-03-29
G1	1996-06-28	180	11.03	1996-06-27	1996-08-09
G2	1996-09-07	251	10.65	1996-09-06	1996-10-07
C3	1996-11-06	311	9.21	1996-11-04	1996-11-27
E4	1996-12-19	354	9.16	1996-12-19	1997-01-04
J5	1997-01-20	20	9.05		1997-02-04
E6	1997-02-20	51	9.12	1997-02-20	1997-03-14
G7	1997-04-04	94	9.12	1997-04-05	1997-04-21
G8	1997-05-08	128	9.27	1997-05-07	1997-06-02
C9	1997-06-27	178	10.77	1997-06-25	1997-08-08
C10	1997-09-18	261	9.17	1997-09-17	1997-10-13
E11	1997-11-06	310	9.03	1997-11-06	1997-11-26
E12	1997-12-16	350	8.80	1997-12-16	1997-12-20
J13	1998-02-10	41	8.85		1998-03-06
E14	1998-03-29	88	8.83	1998-03-29	1998-04-30
E15	1998-06-01	152	8.85	1998-05-31	1998-06-26
E16	1998-07-20	201	9.93		1998-08-23
E17	1998-09-26	269	8.91		1998-10-24
E18	1998-11-22	326	9.23		1998-12-27
E19	1999-02-01	32	9.24	1999-02-01	1999-03-18
C20	1999-05-03	123	9.37		1999-06-02
C21	1999-07-02	183	7.27		1999-07-22
C22	1999-08-12	224	7.32		1999-08-29
C23	1999-09-14	257	6.55		1999-09-27
I24	1999-10-11	284	5.68	1999-10-11	1999-11-01
I25	1999-11-26	330	5.94		1999-12-15
E26	2000-01-04	4	5.78	2000-01-03	2000-01-28
I27	2000-02-22	53	5.85	2000-02-22	2000-04-06
G28	2000-05-21	142	6.68	2000-05-20	2000-09-08
G29	2000-12-29	365	7.49	2000-12-28	2001-03-11
C30	2001-05-23	143	7.28	2001-05-25	2001-06-29
I31	2001-08-06	218	5.93	2001-08-06	2001-09-10
I32	2001-10-15	288	5.78	2001-10-16	2001-12-01
I33	2002-01-17	17	5.54	2002-01-17	2002-06-13
A34	2002-11-05	309	1.99	2002-11-05	2003-04-14
J35	2003-09-21	264	1.00		

Figure 2: Dates associated with orbit numbers. (Adapted from *Joy* (2009).)

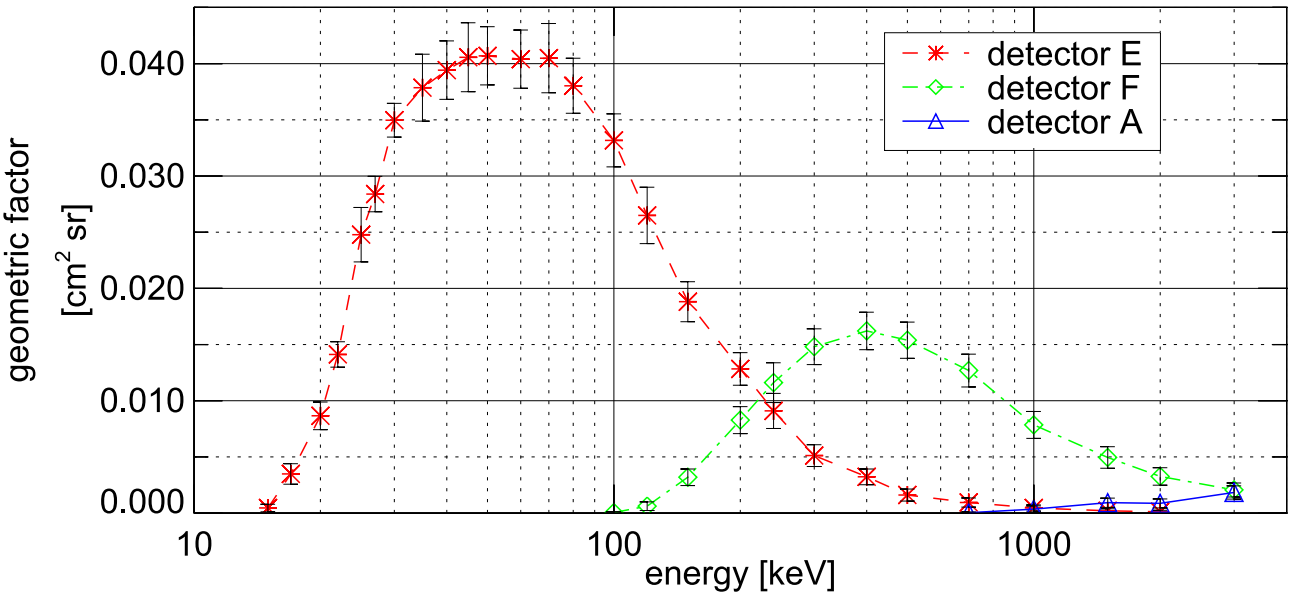

Figure 3: Response functions of the E, F, and A detectors to electrons entering through the LEMMS LET aperture. These response functions were calculated by tracing electrons through the magnetic field of the LET (*Lagg*, 1998). Accounting for energy loss or pulse height defects is not necessary here, meaning that ambient energy of the electrons equals the deposited energy in the SSDs. Response functions for the E1-F3 channels can be calculated by setting the response outside of the energy range of the respective channel (Tab. 1) to zero. The F0 channel adds the contributions of the E and F detectors over its energy range.

at energies outside the channel passband is sufficiently high, that the total count rate may be dominated by energies outside of the passband, even if the channel is much more responsive to energies within its passband. This is true because the count rate relies on the intensities at each energy multiplied by the response function at each energy A proper calculation of intensity spectra therefore should use the full response functions referred to in the table and use a technique similar as described in Sec. 4.3.

The columns labeled with Q and M describe the typical charge and species measured by the channel, respectively. These are either expressed as multiples of the elemental charge or atomic mass units, or labeled with names. It can be seen that sometimes only lower limits are provided. The A channels with $M > 1$ are dominated by $M = 1$ for $L \gtrsim 15$ but have at least comparable contributions of protons and heavier species at smaller distances. (Based on the deconvolved spectra from *Mauk et al.* (2004) and the energy ranges from Tab. 1). ”all” means that all particles are counted that are able to trigger the involved detectors. ”pntr” also refers to all particles but requires that they penetrate the instrument instead of entering through its aperture, which requires high energies.

Some channel definitions changed over the mission and we provide the time ranges in the ”begin” and ”end” columns. The abbreviation DOY means day of year and is counted from day 1 on. This is important when trying to convert DOY into fractional year, where DOY 1 is year.0 (for example 1997.0) not year+1/365 (1997.0027).

The ”HGA sect” and ”LGA sect” columns describe the time resolution while EPD was record or real time mode (HGA_Flag=1 or 0) through the number of sectors into which each channel was binned into. See Sec. 2.5 for details. The columns ”low LGA” to ”high HGA” describe if the data during LGA/HGA mode is available in the low/medium/high files. See Sec. 2.5 for details.

Most EPD channels use the measurements of several detectors in coincidence and/or anticoincidence in order to identify a particle. Each particle causes a pulse in the instrument electronics that is compared against various threshold values. For example, in order to measure an upper limit on the energy of the incident particle it is usually required that a certain detector did not receive a pulse above a threshold. The “logic” column in the tables explains the thresholds that need to be triggered in order for a particle to be counted by a given channel. The column entries provide the detector name (like A, E_1, J, etc., see Fig. 1 for their locations) followed by the threshold number. Detector names J and K refer to both the detectors Ja and Ka, and Jb and Kb of the two EPD/CMS/DeltaExE telescopes (Fig. 1). Detectors E1 and F1 are the upper layer of a stack. Its lower layer is detector E2F2. ST and SP refer to the start and stop MCP anodes. A blank space towards the next entry means a logical AND. A semicolon means OR. An entry in brackets means that this detector/threshold is required to

NOT trigger. For example “E11 (E2)” means that threshold 1 of detector E1 needs to be triggered but that none of the thresholds of detector E2 are allowed to be triggered.

2.4 Best guess channels

Below is a best guess of channels to be used. Measurements always can have artifacts despite all the cleaning that has been done (Sec. 4), meaning that the best guess may not always be the best solution.

Protons: TP1-3. At times where spectra of TP1-TP3 and A1-7 are consistent, one can add A1-7 to the proton set to increase the energy range.

Oxygen: TO2-4

Sulfur: TS1-3

Oxygen and sulfur: TOS1-4

Electrons: E1-E3, F1-F3, FM0-5

2.5 Available resolutions

Due to the failure of Galileo’s high gain antenna, the bulk of the data are only available in low time and directional resolution. This set is referred to as “real time” or ”LGA” data. At times, around close moon flybys and at a series of other times, there were also data taken with higher resolution. This set is referred to as ”record mode” or ”HGA data”. It is described in *Jaskulek and Crane* (1993). As Galileo data is not available continuously, there are gaps in the time series of all modes. In our data files (Sec. 3), we will tag the HGA and LGA time periods by values 1 and 0 in the column *HGA_Flag*.

For each measurement interval, EPD bins measurements from different directions into sectors. The more sectors, the higher the directional resolution. Because different directions are scanned for different times due to the spacecraft spin and instrument motion, binning in direction is equivalent to binning in time.

Both the LGA and HGA modes have each a submode that covers the full range of energies and species available to EPD but has a low time and directional resolution (LGA-0 and HGA-16 modes). Another submode does the opposite and provides high time and directional resolution while only covering a limited energy and species range with reduced energy resolution (LGA-16 and HGA-64). There also exist a third, intermediate submode (LGA-6 and HGA-32). The HGA and LGA columns in Tab. 1-2 refer to the number of sectors that were set up in record and real-time mode, respectively. The LGA mode with 1 sector refers omnidirectional measurements of the foreground. Additionally, there is a measurement of the background taken behind the calibration shield. So this mode has technically 2 sectors, even though the background sector is often not mentioned.

LGA and HGA modes are mutually exclusive and were initially handled as separate data sets. The files provided here combine LGA and HGA data. They combine LGA-0 and HGA-16 data into the **”low_res” low resolution file**, LGA-6 and HGA-32 data into the **”med_res” medium resolution file**, and LGA-16 and HGA-64 data into the **”high_res” high resolution file**. Some files downsample data, meaning that some data were binned to lower time resolution than they are available in. We usually do not interpolate data to higher time/directional resolution. Overall, this means that the low resolution files includes all channels. These channels are either provided at their native resolution or are downsampled. Higher resolution data may be found in the high and medium files. The high resolution file is genuine high resolution data, provided at its native resolution, but only includes a subset of channels.

The content of the low, medium, and high files during times with HGA and LGA data are spelled out in Tab. 1-2 in the columns low HGA, low LGA, med HGA, med LGA, high HGA, high LGA. ”Full” indicates in which file and during which mode the highest available resolution of a channel can be found. ”Bin” means that the channel is included in the respective file at the respective HGA/LGA mode but that it is provided with downsampled resolution.

A channel might be available only in lower time resolution than required for the respective medium or high resolution file. If this only occurs in textiteither LGA *or* HGA mode, we fill in such instances with NaN/-1.000000E+38 values because we only bin but usually not interpolate data. Such instances are labeled with ”Nan” in the table. If the channel would need to be set as Nan for *both* in HGA *and* LGA mode, we do not list that channel at all in the data file. Such cases are labeled with ”Not” in the table.

name	instr.	geo.fact [cm^2 sr]	Q	M	low [keV]	center [keV]	high [keV]	begin year/DOY	end year/DOY	HGA sect	LGA sect	low HGA	low LGA	med HGA	med LGA	high HGA	high LGA	logic	footnote Tab. 4
A0	LET	0.0052	≥ 1	≥ 1	22	30	42	1990/350	1997/305	64	6	bin	bin	bin	full	full	Nan	A1 (A2 B1)	1
A0	LET	0.0052	≥ 1	≥ 1	34	38	42	1997/305	2004	64	6	bin	bin	bin	full	full	Nan	A1 (A2 B1)	1
A1	LET	0.0056	≥ 1	≥ 1	42	52	65	1988	2004	64	16	bin	bin	bin	bin	full	full	A2 (A3 B1)	1
A2	LET	0.006	≥ 1	≥ 1	65	88	120	1988	2004	32	16	bin	bin	full	bin	Nan	full	A3 (A4 B1)	1
A3	LET	0.006	≥ 1	≥ 1	120	183	280	1988	2004	32	6	bin	bin	full	full	not	not	A4 (A5 B1)	1
A4	LET	0.006	≥ 1	≥ 1	280	380	515	1988	2004	32	6	bin	bin	full	full	not	not	A5 (A6 B1)	1
A5	LET	0.006	≥ 1	≥ 1	515	652	825	1988	2004	32	6	bin	bin	full	full	not	not	A6 (A7 B1)	1
A6	LET	0.006	≥ 1	≥ 1	825	1177	1680	1988	2004	32	6	bin	bin	full	full	not	not	A7 (A8 B1)	1
A7	LET	0.006	≥ 1	≥ 1	1680	2319	3200	1988	2004	32	6	bin	bin	full	full	not	not	A8 (A9 B1)	1
A8	LET	0.006	≥ 2	≥ 4	3480	5342	8200	1988	2004	16	6	full	bin	Nan	full	not	not	A9 (B1 C2)	2
E0	LET	0.015	-1	e	15	21	29	1988	2004	64	6	bin	bin	bin	full	full	Nan	E11 (E12 E2)	3
E1	LET	0.038	-1	e	29	35	42	1988	2004	64	16	bin	bin	bin	bin	full	full	E12 (E13 E2)	3
E2	LET	0.04	-1	e	42	48	55	1988	2004	32	6	bin	bin	full	full	not	not	E13 (E14 E2)	3
E3	LET	0.038	-1	e	55	72	93	1988	2004	32	6	bin	bin	full	full	not	not	E14 (E15 E2)	3
F0	LET	0.025	-1	e	93	132	188	1988	2004	32	6	bin	bin	full	full	not	not	E15 (E16 E2); F11 (F12 F2)	3
F1	LET	0.017	-1	e	174	230	304	1988	2004	32	6	bin	bin	full	full	not	not	F12 (F13 F2)	3
F2	LET	0.016	-1	e	304	400	527	1988	2004	32	16	bin	bin	full	bin	Nan	full	F13 (F14 F2)	3
F3	LET	0.012	-1	e	527	683	884	1988	2004	32	6	bin	bin	full	full	not	not	F14 (F15 F2)	3
B0	LET	0.0095	1	H	3500	5916	10000	1988	2004	16	1	full	bin	Nan	full	not	not	A7 B1 (C2)	4; 4b
B1	LET	?	-1	e	?	-	∞	1988	2004	16	1	full	bin	Nan	full	not	not	A2 (A4) B1 (B2 C2)	4, 4c
B2	LET	0.006	≥ 1	≥ 4	16000	40000	100000	1988	2004	16	1	full	bin	Nan	full	not	not	A8 B3 (C2)	2; 4b
DC0	HET	0.005	± 1	e+H	14000	-	∞	1988	2004	16	1	full	full	not	not	not	not	(B1) D2 (C1)	4; 4b; 5
DC1	HET	0.005	± 1	e	30000	-	∞	1988	2004	16	1	full	full	not	not	not	not	(B1) C2 D1	4; 5
DC2	HET	0.58	-1	e	1800	-	∞	1988	2004	16	1	full	full	not	not	not	not	(B1) D1 (D2)	4
DC3	HET	0.27	-1	e	10800	-	∞	1988	2004	16	1	full	full	not	not	not	not	(B1) C1 (C2) D1	4
As	LET	0.006	all	all	22	-	∞	1988	1997/305	16	6	full	bin	Nan	full	not	not	A1	6
As	LET	0.006	all	all	34	-	∞	1997/305	2004	16	6	full	bin	Nan	full	not	not	A1	6
Bs	LET	0.006	all	all	> 75	?	∞	1988	2004	16	6	full	bin	Nan	full	not	not	B1	6; 7
Cs	HET	0.42	all	all	> 162	?	∞	1988	2004	16	1	full	full	not	not	not	not	C1	6; 7
Ds	HET	0.42	all	all	> 133	?	∞	1988	2004	16	1	full	full	not	not	not	not	D1	6; 7
EB1	LET	?	all	pntr.	?	-	∞	1988	2004	16	1	full	full	not	not	not	not	E16 (E2)	6
EB2	LET	?	all	pntr.	?	-	∞	1988	2004	16	1	full	full	not	not	not	not	E11 E2	6
FB1	LET	?	all	pntr.	?	-	∞	1988	2004	16	1	full	full	not	not	not	not	F15 (F2)	6
FB2	LET	?	all	pntr.	?	-	∞	1988	2004	16	1	full	full	not	not	not	not	F11 F2	6

Table 1: Galileo/EPD/LEMMS channel parameters. See Sec. 2.3-2.5 for column explanations.

name	instr.	geo. fact [cm^2 sr]	Q	M	low [keV]	center [keV]	high [keV]	begin year	end year	HGA sect	LGA sect	low HGA	low LGA	med HGA	med LGA	high HGA	high LGA	logic	footnote Tab. 4
TP1	TOFxE	0.001	1	H	130	169	220	1988	1996	16	16	full	bin	Nan	bin	Nan	full	ST SP KT	8; 10; 20
TP1	TOFxE	0.001	1	H	80	133	220	1996	1999	16	16	full	bin	Nan	bin	Nan	full	ST SP KT	8; 10; 19
TP1	TOFxE	< 0.001	1	H	115	167	244	1999	2004	16	16	full	bin	Nan	bin	Nan	full	ST SP KT	18
TP2	TOFxE	0.0011	1	H	220	345	540	1988	1999	16	16	full	bin	Nan	bin	Nan	full	ST SP KT	9; 10; 19
TP2	TOFxE	< 0.0011	1	H	244	369	558	1999	2004	16	16	full	bin	Nan	bin	Nan	full	ST SP KT	18
TP3	TOFxE	0.0006	1	H	540	785	1140	1988	1999	16	6	full	bin	Nan	full	not	not	ST SP KT	10; 19
TP3	TOFxE	< 0.0006	1	H	558	803	1155	1999	2004	16	6	full	bin	Nan	full	not	not	ST SP KT	18
TA1	TOFxE	0.0025	all	He	108	259	620	1988	1999	16	16	full	bin	Nan	bin	Nan	full	ST SP KT	10; 19
TA1	TOFxE	< 0.0025	all	He	183	350	673	1999	2004	16	16	full	bin	Nan	bin	Nan	full	ST SP KT	18
TA2	TOFxE	0.003	all	He	620	1575	4000	1988	1999	16	6	full	bin	Nan	full	not	not	ST SP KT	10; 19
TA2	TOFxE	< 0.003	all	He	673	1640	4000	1999	2004	16	6	full	bin	Nan	full	not	not	ST SP KT	18
TO1	TOFxE	0.001	all	O+S	235	283	416	1988	1996	16	16	full	bin	Nan	bin	Nan	full	ST SP KT	11; 10; 20
TO1	TOFxE	0.001	all	O+S	192	283	416	1996	1999	16	16	full	bin	Nan	bin	Nan	full	ST SP KT	12; 10; 19
TO1	TOFxE	< 0.001	all	O+S	> 192	> 283	> 416	1999	2004	16	16	full	bin	Nan	bin	Nan	full	ST SP KT	21
TO2	TOFxE	0.0025	all	O	416	583	816	1988	1999	16	16	full	bin	Nan	bin	Nan	full	ST SP KT	10; 19
TO2	TOFxE	< 0.0025	all	O+S	> 416	> 583	> 816	1999	2004	16	16	full	bin	Nan	bin	Nan	full	ST SP KT	21
TO3	TOFxE	0.0035	all	O	816	1209	1792	1988	1999	16	16	full	bin	Nan	bin	Nan	full	ST SP KT	10; 19
TO3	TOFxE	< 0.0035	all	O+S	> 816	> 1209	> 1792	1999	2004	16	16	full	bin	Nan	bin	Nan	full	ST SP KT	21
TO4	TOFxE	0.0035	all	O	1792	4014	8992	1988	1999	16	6	full	bin	Nan	full	not	not	ST SP KT	10; 19
TO4	TOFxE	< 0.0035	all	O+S	> 1792	> 4014	> 8992	1999	2004	16	6	full	bin	Nan	full	not	not	ST SP KT	21
TS1	TOFxE	0.002	all	S	512	701	960	1988	1999	16	16	full	bin	Nan	bin	Nan	full	ST SP KT	10; 19
TS1	TOFxE	$<< 0.002$	all	S	> 512	> 701	> 960	1999	2004	16	16	full	bin	Nan	bin	Nan	full	ST SP KT	21
TS2	TOFxE	0.003	all	S	960	1380	1984	1988	1999	16	16	full	bin	Nan	bin	Nan	full	ST SP KT	10; 19
TS2	TOFxE	$<< 0.003$	all	S	> 960	> 1380	> 1984	1999	2004	16	16	full	bin	Nan	bin	Nan	full	ST SP KT	21
TS3	TOFxE	0.0035	all	S	1984	4436	9920	1988	1999	16	6	full	bin	Nan	full	not	not	ST SP KT	10; 19
TS3	TOFxE	$<< 0.0035$	all	S	> 1984	> 4436	> 9920	1999	2004	16	6	full	bin	Nan	full	not	not	ST SP KT	21
TH1	TOFxE	0.003	all	$M \gg 32$	1120	3542	11200	1988	2004	16	6	full	bin	Nan	full	not	not	ST SP KT	13
TACs	TOFxE	0.007	all	all	?	-	∞	1988	2004	16	6	full	bin	Nan	full	not	not	ST SP	6
KTs	TOFxE	?	all	all	?	-	∞	1988	2004	16	6	full	bin	Nan	full	not	not	KT	6
START	TOFxE	?	all	all	?	-	∞	1988	2004	16	16	full	bin	Nan	bin	Nan	full	ST	6
CA1	DeltaExE	0.008	all	He	760	1220	1960	1988	2004	16	-	full	Nan	not	not	not	not	J (K)	14
CA3	DeltaExE	0.008	all	He	1960	2309	2720	1988	2004	16	-	full	Nan	not	not	not	not	J K	14
CA4	DeltaExE	0.008	all	He	2720	3903	5600	1988	2004	16	-	full	Nan	not	not	not	not	J K	14
CM1	DeltaExE	0.008	all	O	2560	4746	8800	1988	2004	16	-	full	Nan	not	not	not	not	J (K)	14
CM3	DeltaExE	0.008	all	O	8800	12445	17600	1988	2004	16	-	full	Nan	not	not	not	not	J K	14
CM4	DeltaExE	0.008	all	O	17600	28577	46400	1988	2004	16	-	full	Nan	not	not	not	not	J K	14
CM5	DeltaExE	0.008	all	O	46400	89127	171200	1988	2004	16	-	full	Nan	not	not	not	not	J K	14
CN0	DeltaExE	0.008	all	≈ 23	23000	34115	50600	1988	2004	16	-	full	Nan	not	not	not	not	J K	14
CN1	DeltaExE	0.008	all	≈ 23	50600	116690	269100	1988	2004	16	-	full	Nan	not	not	not	not	J K	14
CH1	DeltaExE	0.008	all	S	7040	8622	10560	1988	2004	16	-	full	Nan	not	not	not	not	J (K)	14,17
CH3	DeltaExE	0.008	all	S	10560	15047	21440	1988	2004	16	-	full	Nan	not	not	not	not	J K	14,17
CH4	DeltaExE	0.008	all	S	21440	29865	41600	1988	2004	16	-	full	Nan	not	not	not	not	J K	14,17
CH5	DeltaExE	0.008	all	S	41600	141308	480000	1988	2004	16	-	full	Nan	not	not	not	not	J K	14,17
Jas	DeltaExE/A	0.008	all	all	?	?	?	1988	2004	16	-	full	Nan	not	not	not	not	Ja	6
Jbs	DeltaExE/B	0.025	all	all	?	?	?	1988	2004	16	-	full	Nan	not	not	not	not	Jb	6
Ks	DeltaExE	0.034	all	all	?	?	?	1988	2004	16	-	full	Nan	not	not	not	not	K	6

Table 2: Galileo/EPD/CMS channel parameters. See Sec. 2.3-2.5 for column explanations.

name	instrument	geo. fact [cm^2 sr]	charge	species	low [keV]	center [keV]	high [keV]	begin year	end year	HGA sect	LGA sect	low HGA	low LGA	med HGA	med LGA	high HGA	high LGA	logic	footnote Tab. 4
DC2F	LEMMS	-	-1	e	-	1800	-	1988	2004	16	1	NAN	full	not	not	not	not	F1-F3,DC2-3,B1	15
DC3F	LEMMS	-	-1	e	-	10800	-	1988	2004	16	1	NAN	full	not	not	not	not	F1-F3,DC2-3,B1	15
FM0F	LEMMS	-	-1	e	-	1800	-	1988	2004	16	1	NAN	full	not	not	not	not	F1-F3,DC2-3,B1	15
FM1F	LEMMS	-	-1	e	-	2010	-	1988	2004	16	1	NAN	full	not	not	not	not	F1-F3,DC2-3,B1	15
FM2F	LEMMS	-	-1	e	-	4489	-	1988	2004	16	1	NAN	full	not	not	not	not	F1-F3,DC2-3,B1	15
FM3F	LEMMS	-	-1	e	-	10025	-	1988	2004	16	1	NAN	full	not	not	not	not	F1-F3,DC2-3,B1	15
FM4F	LEMMS	-	-1	e	-	22388	-	1988	2004	16	1	NAN	full	not	not	not	not	F1-F3,DC2-3,B1	15
FM5F	LEMMS	-	-1	e	-	50000	-	1988	2004	16	1	NAN	full	not	not	not	not	F1-F3,DC2-3,B1	15
TOS1	CMS/TOFxE	0.001	all	O+S	235	283	416	1996	2004	16	16	full	bin	Nan	bin	Nan	full	TO1	16
TOS1	CMS/TOFxE	0.001	all	O+S	192	283	416	1996	2004	16	16	full	bin	Nan	bin	Nan	full	TO1	16
TOS2	CMS/TOFxE	0.0025	all	O+S	416	583	816	1988	2004	16	16	full	bin	Nan	bin	Nan	full	TO2+TS1	16
TOS3	CMS/TOFxE	0.0035	all	O+S	816	1209	1792	1988	2004	16	16	full	bin	Nan	bin	Nan	full	TO3+TS2	16
TOS4	CMS/TOFxE	0.0035	all	O+S	1792	4014	8992	1988	2004	16	6	full	bin	Nan	full	not	not	TO4+TS3	16

Table 3: Artifical Galileo/EPD channel parameters. See Sec. 2.3-2.5 for column explanations.

number	footnote
1	Table here and intensity data assume protons. Channel generally responds to all ions (*Mauk et al.*, 2004)
2	Table here and intensity data assume helium. Channel generally responds to all non-proton ions (*Mauk et al.*, 2004)
3	Values here are from *Lagg* (2004). Full response and effective geometry factors assuming non-flat spectra are shown in *Lagg* (1998) and Fig. 3
4	Full response in *Jun et al.* (2002)
4b	Full response in *Martinez Sierra et al.* (2015)
4c	poorly defined onset of response: 50% of maximum geometry factor at $>$ 36MeV, 10% at $>$ 0.8MeV
5	Table here and intensity data assume purely electrons. Channel was also designed to respond to protons.
6	Only for diagnostic purposes
7	Table energies are deposited in solid state detector
8	Intensity data are based on the energy range in the table. Channel additionally responds to 3870-16000keV protons.
9	Intensity data are based on the energy range in the table. Channel additionally responds to 1140-3870keV protons.
10	Full response in *Mauk et al.* (2004) (use their Fig. A1 or multiply their Tab. A2 with 0.533)
11	Table here and intensity data assume oxygen. Channel responds similarly to 310-512keV sulfur.
12	Table here and intensity data assume oxygen. Channel responds similarly to 253-512keV sulfur.
13	Contaminated channel that should not be used as calibrated.
14	Geometry factor was 0.034 cm^2 sr before 1997 DOY 234
15	Based on forward model (Sec. 4.3)
16	Sums the count rates and calibrates them as oxygen
17	Energy ranges provided in an earlier version of this table (*Kollmann et al.*, 2018) were assuming Fe, which is wrong
18	Energy range modified to account for instrument degradation (Sec. 4.4, *Lee-Payne et al.* (2020)).
19	Nominal energy range, without instrument degradation.
20	Non-standard energy threshold that was used during JOI and possibly before (*Mauk et al.*, 2004).
21	Oxygen and sulfur are not properly separated anymore in the later mission (Sec. 4.4, *Lee-Payne et al.* (2020)).
22	No well-defined response. It ramps up slowly from 10% of the maximum value of 0.02cm^2 sr at 1MeV to 50% at 36MeV (*Jun et al.*, 2002).

Table 4: Footnotes to Tab. 1 - 3.

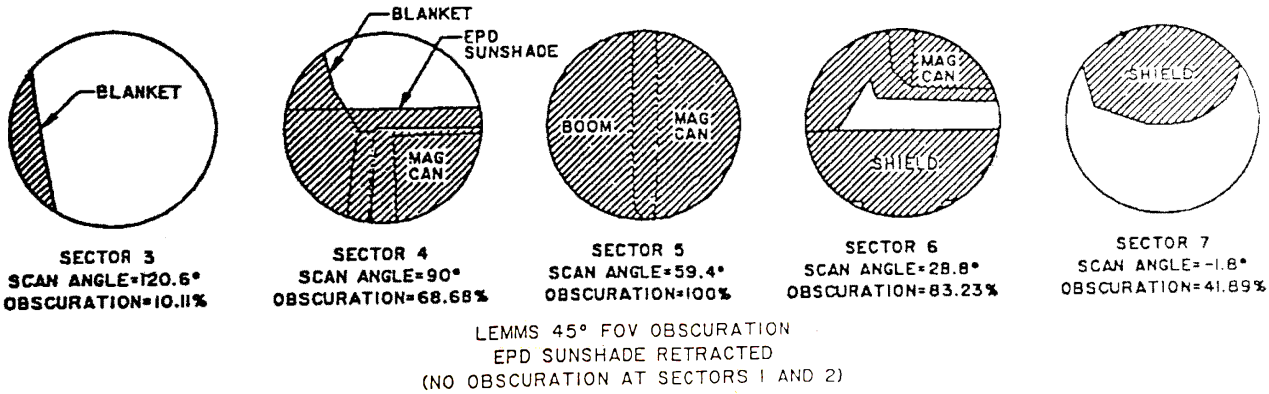

Figure 4: Obscuration of EPD/LEMMS/HET. "Sector" in the labels is equal to motor position. EPD/LEMMS/LET does not have a known obscuration.

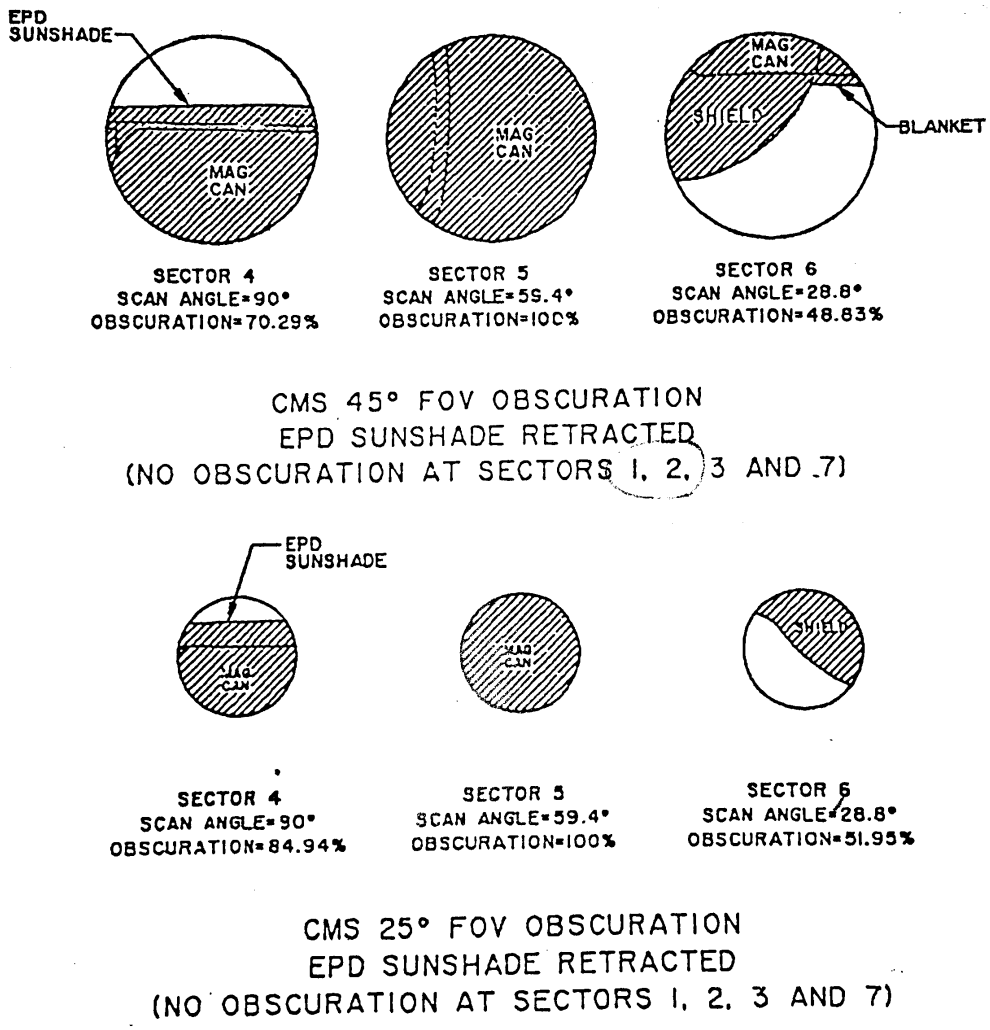

Figure 5: Obscuration of EPD/CMS/DeltaExE/B and A. "Sector" in the labels is equal to motor position. EPD/LEMMS/CMS/TOFxE does not have a known obscuration.

2.6 Calibration shield and motor step

This section explains details on the orientation and look direction of the EPD instrument. It is only necessary to read if pitch angles do not provide sufficient directional information for the desired application.

EPD was mounted on a platform that performed discrete steps (different to a continuous rotation) between position numbered from 0 to 7. In step 0, the LET was placed behind a calibration shield. The HET does not fully go behind the calibration shield but suffers obscuration that maximizes in step 5 (Fig. 4 and 5).

The Galileo spin rate was about 20s, so that with the combination of spin and the stepping motor, it was possible to gain access to many look directions.

In HGA mode, when *HGA_flag*=1, **step** is the actual motor position. It always goes from 0-7.

In HGA mode the spin was split over 16 spin phase values illustrated in Fig. 8. Spin phase and motor position and then combined into spin sectors that describe regions in the sky as illustrated in Fig. 8. Spin phase and spin sector are not always clearly distinguished in the documentations. The **spin** sector range is 0-15 for HGA-16, 0-31 for HGA-32, and 0-63 for HGA-64. The spin sector is not directly provided in the raw binary data files but calculated from the lemms.astepb.mstep variable. Note that other data sets sometimes start counting at 1 instead of 0.

In LGA mode, when *HGA_flag*=0, the spin phase has different ranges. For LGA-6 and LGA-16 (medium and high resolution files, see Sec. 2.5) **spin** ranges from 0-3, sometimes labeled as A-D (like in Fig. 9). When spin phases are averaged together, they are labeled as the lowest spin phase. For LGA-1 (low resolution file) *spin* is always 0 because data of all spin phases was averaged together.

In LGA mode **step** labels the motor positions but accounts for some steps being summed together. For LGA-16 the *step* range is 1-5 because the actual position 0 is excluded and positions 1 and 2 are summed together (Fig. 9), leaving only 5 effective steps. For LGA-6 the range is 0-3 because the actual positions 1+2 and 3+4+5 are summed. In LGA-1 the instrument is measuring foreground (motor positions 1+2+3+4+5+6 summed into omnidirectional measurements, sometimes referred to as o1) and data behind the calibration shield (motor position 0, sometimes refereed to as m1, and provided in the columns ending with BG as described in Sec. 3.3.2).

2.7 Event Data

The instrument channels discussed so far count all measured particles within coarse bins in energy and species. Event data are different than the channel data discussed above because they record the full information of a measured particle. Every ”event” is the measurement of a TOF and energy value (EPD/CMS/TOFxE), or two energy values (EPD/CMS/DeltaExE), see Fig. 23. Event data provides these values in the native resolution of the instrument. Channelized data in comparison bin these values into relatively large intervals. These intervals are outlined as black lines in Fig. 23. Values of the corner points of the CMS channels are listed in Tab. 5-7. These points can be used to determine into which channel an event falls.

Event data are large data products because they are not channelized or otherwise averaged. Therefore event data cannot be taken continuously and downlinked all the time. Only a subset of this data is kept.

There are two applications for event data: 1) They can be used to determine energy spectra with high energy resolution. However, event data trade energy resolution against time resolution, which can be problematic. Typically a long time is needed to accumulate enough counts, during which the spacecraft is changing location, potentially smearing out spectral signatures. 2) Event data are useful to understand and illustrate some instrumental issues. This will be used in the discussion in Sec. 4.2 and 4.4.

There can be artificial jumps in the event data count rates between different regions in TOF vs. energy space. For example, there are usually more event data counts in TO3 than in TO2 (see for example right panel in Fig. 13), even though TO3 measures higher energies and therefore should have a lower count rate. In fact, the rate at which event are taken in TO3 would be so low that the channel would be barely populated. In order to avoid this, EPD uses a priority scheme. The nature of a priority scheme is that it artificially prioritizes certain portions of the TOFxE matrix that otherwise would be underpopulated. Each channel is assigned a priority number (Fig. 10, left panel). After one event with a certain priority number is recorded and/or transmitted, the instrument waits until an event with a certain other priority number arrives until it records/transmits another event. What number the instrument waits for is described in Fig. 10, right panel. Fig. 15 left shows clearly the locations of CMS/TOFxE channels in the TOFxE matrix.

In order to convert event count rates to intensities, the event counts of each channel first need to be scaled so that they match the counts of the respective channel. Afterwards, the counts need to be binned in energy,

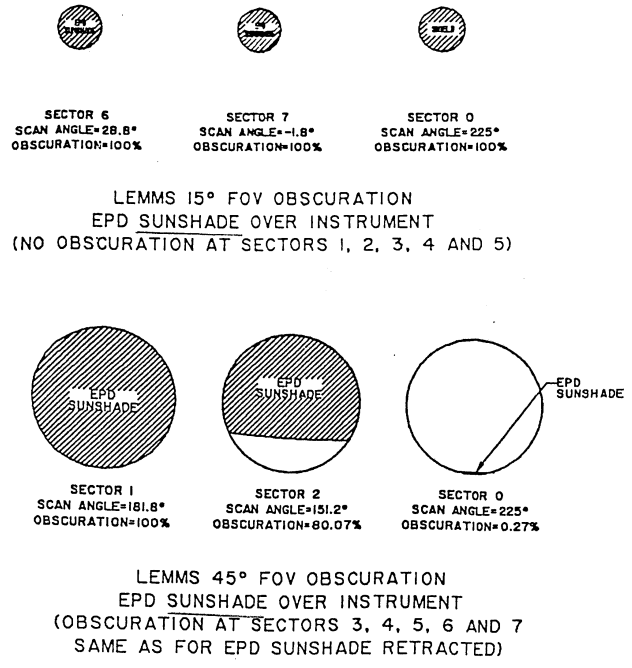

Figure 6: Obscuration of EPD/LEMMS/LET and HET while the sunshade was on. This was not the case for the published data but is documented here for completeness.

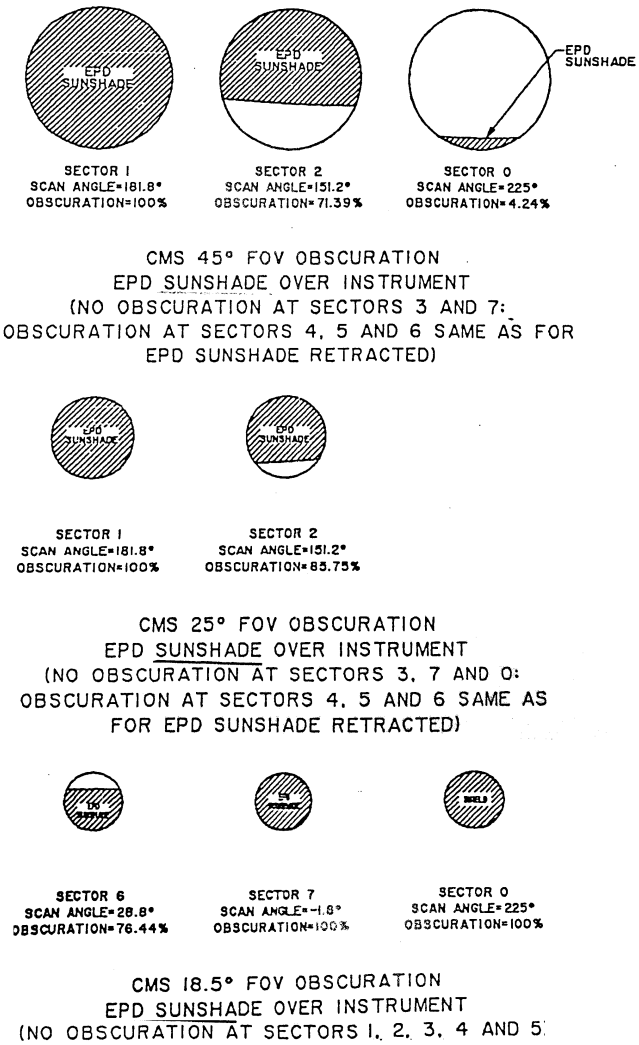

Figure 7: Obscuration of EPD/CMS/DeltaExE/B, EPD/CMS/DeltaExE/A, and EPD/CMS/TOFxE while the sunshade was on. This was not the case for the published data but is documented here for completeness.

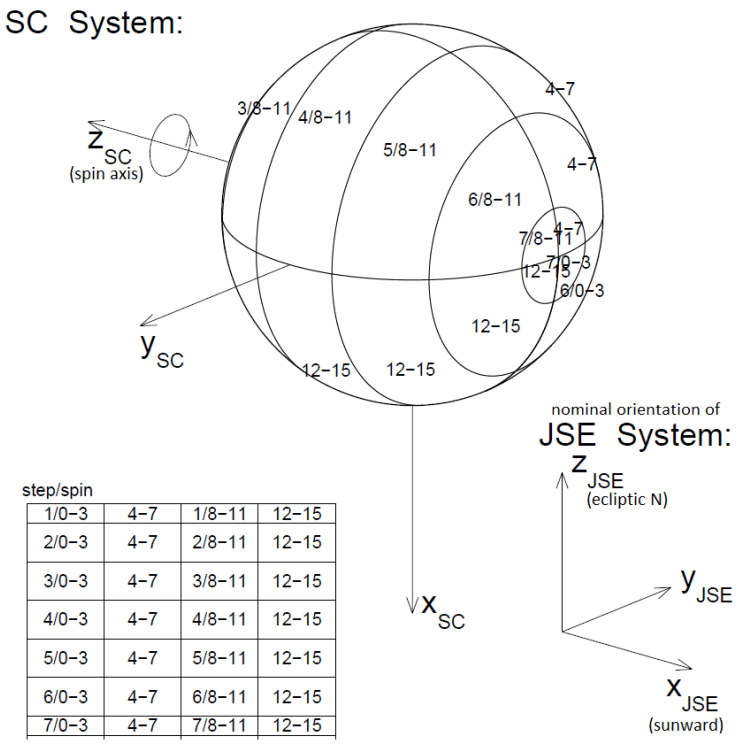

step/spin

1/0−3	4−7	1/8−11	12−15
2/0−3	4−7	2/8−11	12−15
3/0−3	4−7	3/8−11	12−15
4/0−3	4−7	4/8−11	12−15
5/0−3	4−7	5/8−11	12−15
6/0−3	4−7	6/8−11	12−15
7/0−3	4−7	7/8−11	12−15

Figure 8: Averaging of instrument motor steps and spacecraft spin sectors in the HGA-32 mode (*Lagg*, 1998). Motor step 0 that points the LET toward the calibration shield is not shown here. "0-3" means that spin steps 0 through 3 are averaged together, both for the HGA-32 data product and in the illustration of the figure. HGA-16 and 64 average over twice and half the number of spin sectors, respectively. The nominal orientation between spacecraft and JSE system is also shown. The actual attitude can deviate.

LGA − 1

Spin Sector	Motor Position						
	0	1	2	3	4	5	6
A	c1	c2					
B							
C							
D							

LGA − 6

Spin Sector	Motor Position						
	0	1	2	3	4	5	6
A	b1	b2		b3			b7
B				b4			
C				b5			
D				b6			

LHA − 16

Spin Sector	Motor Position						
	0	1	2	3	4	5	6
A	a1	a2		a4	a5	a6	a16
B				a7	a8	a9	
C		a3		a10	a11	a12	a17
D				a13	a14	a15	

Figure 9: Averaging of spacecraft Spin sectors and instrument Motor Position in LGA mode.

divided by the size of the intervals in energy and time, and divided by the energy dependent geometry factor and efficiency (*Mauk et al.* (2004), use their Fig. A1 or multiply their Tab. A2 with 0.533).

3 Data files content

3.1 File types

The low_res, med_res, and high_res files in the epd_channels folder include LEMMS and CMS rate channels (Sec. 2.3), which is most likely what you want to use. Each file combines record and real time mode. The higher the resolution (in time and direction) the smaller the coverage in energy, species, and time. Details on resolutions are given in Sec. 2.5.

The cms_deltaexe and cms_tof files in the cms_events folder include CMS event data, which are most useful for diagnostic purposes (Sec. 2.7).

Data files are in the Comma Separated Value (CSV) format. All file types delivered to the PDS are split in yearly files. Each data file is accompanied by a label file that describe the content of the data files including file structure, processing status, and calibration. The PDS4 standard uses EXtensible Markup Language (XML) format for the label files.

3.2 File format

Data are stored as comma separated plain text files.

Sec. 3.3 describes the data files for the channelized data (see Sec. 2.3 for a general explanation), which is most likely what you want to use. Sec. 3.4 describes the data files for the event data (that were introduced in Sec. 2.7).

Invalid entries will have -1.000000E+38 as a value. Invalid entries mean that there is no usable measurement, which is different to for example a valid measurement that showed zero counts. It is crucial that invalid values are not included in the analysis, particularly not averaged together with valid values. It is suggested to replace these values immediately with Not-a-Number (NAN) values. It was not possible to implement this here due to restrictions of the PDS format.

Negative intensity values tag times where the data may be unreliable for different reasons explained in Sec. 4.2. Negative and invalid values should be removed before detailed analysis, particularly before calculating average values.

3.3 EPD channels low to high resolution files

3.3.1 Header

The first 4 lines of each rate text file provide information on the rate channels included. The first two lines list the channel energies: The first line lists the names of the channels included here, each channel followed by the letter "E". The second line lists the center energies of these channels in keV. The second two lines list the main species: The third line in the file lists the channels again, each channel followed by the letter "S". The fourth line lists the most likely mass of the measured particle in AMU. Zero mass refers to electrons. These masses are not always correct and can deviate for small L-shells, see the "M" columns in Tab. 1-4 and the discussion in Sec. 2.3. More detailed information on these channels (like for example the energy ranges of the channels) can be found in Tab. 1-2 and in the PDS label files.

The fifth line in the data text file labels the columns that follow in the file. The columns include times (Sec. 3.3.3), radiation measurements (Sec. 3.3.2), spacecraft location, instrument look direction, and some supplementary information (Sec. 3.3.3). Details are described below. Each following line will provide the same data but for different times.

3.3.2 Radiation rates and intensities

The data files provide both the raw count rates of the channels (to the right of the file) as well as the best calibrated and cleaned data (to the left). Channels are in alphabetical order.

Columns with **channel names followed by a "J"** (like *E1J*, *TP1J*) include calibrated differential intensities in 1/(keV cm^2 sr s) that were cleaned and corrected. The applied corrections to the data are described in Sec. 4. Intensities are provided as positive values when the measurement is reliable. If the measurement is not reliable

Table 4. New CMS Rate ID and Priority Assignment

RATE ID NUM.	PRIORITY	RATE CHANNELS TOF END		PRIME END
0	I	--		CM5
1	I	--		CN0
2	I	TH1	or	CN1
3	I	--		CH5
4	II	TO3 or TO4		--
5	II	TS2	or	CH3
6	II	TS3	or	CH4
8	III	TO1		--
9	III	TS1	or	CM3
10	III	TO2	or	CM4
12	IV	TP1 or TP2 or TP3		--
13	IV	TA1		CA3
14	IV	TA2		CA4

Priority Ordering After Each Event Transmitted

Category of last event transmitted	I	II	III	IV
Priority for next event transmitted				
(Highest) 1st	II	III	IV	I
2nd	III	IV	I	II
3rd	IV	I	II	III
(Lowest) 4th	I	II	III	IV

Figure 10: Priority scheme for event data of the EPD/CMS instrument. Top: Priority numbers (roman numbers) of the channels (entries like TH1, CM5, etc.). Bottom: Priority scheme determining which events are recorded/transmitted, depending on the priority number of the last recorded/transmitted event.

channel	E_dep [keV]	TOF [ns]
TP1	54.0487	1.28054
TP1	54.0487	14.1424
TP1	208.258	8.51657
TP1	208.258	1.28054
TP2	208.258	1.28054
TP2	208.258	8.51657
TP2	534.200	5.88674
TP2	534.200	1.28054
TP3	534.200	1.28054
TP3	534.200	5.88674
TP3	14465.8	1.45606
TP3	14465.8	1.28054
TA1	54.0487	14.1424
TA1	54.0487	22.9059
TA1	534.200	9.52971
TA1	534.200	5.88674
TA2	534.200	5.88674
TA2	534.200	9.52971
TA2	14465.8	6.37884
TA2	14465.8	2.28264
TO1	54.0487	22.9059
TO1	54.0487	48.6601
TO1	208.258	28.2859
TO1	208.258	13.7225
TO2	208.258	13.7225
TO2	208.258	20.3045
TO2	534.200	14.3572
TO2	534.200	9.52971
TO3	534.200	9.52971
TO3	534.200	14.3572
TO3	1366.70	9.84071
TO3	1366.70	6.37884
TO4	1366.70	6.37884
TO4	1366.70	9.84071
TO4	14465.8	3.57846
TO4	14465.8	2.28264
TS1	208.258	20.3045
TS1	208.258	28.2859
TS1	534.200	19.7017
TS1	534.200	14.3572
TS2	534.200	14.3572
TS2	534.200	19.7017
TS2	1366.70	13.1160
TS2	1366.70	9.84071
TS3	1366.70	9.84071
TS3	1366.70	13.1160
TS3	14465.8	4.62671
TS3	14465.8	3.57846
TH1	54.0487	48.6601
TH1	54.0487	68.8171
TH1	14465.8	68.8171
TH1	14465.8	4.62671

Table 5: Corner points of the EPD/CMS channels, part 1

channel	E_dep [keV]	TOF [ns]
TP2_high	208.258	4.70160
TP2_high	208.258	8.51657
TP2_high	534.200	5.88674
TP2_high	534.200	3.81584
TP2_low	208.258	1.28054
TP2_low	208.258	4.70160
TP2_low	534.200	3.81584
TP2_low	534.200	1.28054
channel	E_K [keV]	E_J [keV]
CA1	97.6405	711.660
CA1	97.6405	2235.52
CA1	365.818	2235.52
CA1	365.818	711.660
CA3	365.818	711.660
CA3	365.818	2235.52
CA3	1453.06	2235.52
CA3	1453.06	711.660
CA4	1453.06	711.660
CA4	1453.06	2235.52
CA4	38793.2	2235.52
CA4	38793.2	711.660
CM1	97.6405	2235.52
CM1	97.6405	10353.7
CM1	365.818	10353.7
CM1	365.818	2235.52
CM3	365.818	2235.52
CM3	365.818	10353.7
CM3	8999.20	10353.7
CM3	8999.20	2235.52
CM4	8999.20	2235.52
CM4	8999.20	10353.7
CM4	19925.1	10353.7
CM4	38793.2	7212.96
CM5	38793.2	711.660
CM5	38793.2	7212.96
CM5	1.00000e+006	1599.66
CM5	1.00000e+006	711.660
CN0	8999.20	10353.7
CN0	8999.20	13899.7
CN0	38793.2	13899.7
CN0	38793.2	7212.96
CN1	38793.2	7212.96
CN1	38793.2	13899.7
CN1	1.00000e+006	3062.04
CN1	1.00000e+006	1599.66

Table 6: Corner points of the EPD/CMS channels, part 2

channel	E_K [keV]	E_J [keV]
CH1	97.6405	10353.7
CH1	97.6405	43082.1
CH1	365.818	43082.1
CH1	365.818	10353.7
CH3	365.818	10353.7
CH3	365.818	43082.1
CH3	8999.20	43082.1
CH3	8999.20	10353.7
CH4	8999.20	13899.7
CH4	8999.20	43082.1
CH4	38793.2	43082.1
CH4	38793.2	13899.7
CH5	38793.2	13899.7
CH5	38793.2	43082.1
CH5	1.00000e+006	43082.1
CH5	1.00000e+006	3062.04

Table 7: Corner points of the EPD/CMS channels, part 3

(due to anomalous periods, dead time, background > foreground, etc.), the intensity is forced to invalid values (-1.000000E+38). If intensities are questionable (because the foreground/background < 4, see Sec. 4.2), their intensity will be negative. Raw measurements will always be provided even if intensity values are negative.

For channels with very wide response functions that may extend essentially to infinite energies, we cannot provide differential intensities based on a single channel. In order to still provide measurements of such channels in physical units, we calculate integral intensities in 1/(cm^2 sr s). These are provided in columns with **channel names followed by a "I"** (like *DC1I*). These integral intensities calculate as

$$I_r = \int_0^\infty \epsilon(E) j(E) \mathrm{d}E \tag{1}$$

With ϵ being the energy-dependent efficiency of the channel, which is proportional to the energy dependent geometry factor. (For references to such factors see Tab. 1-4.) I_r is different to the ideal integral intensity I_i above a sharp threshold energy E_0, even though the units of I_r and I_i are the same.

$$I_i = \int_{E_0}^\infty j(E) \mathrm{d}E \tag{2}$$

We combined several electron channels with wide response functions in order to derive differential intensities at MeV energies (Sec. 4.3). The forward model we used provides differential intensities over a large energy range that we evaluate near the onset energies of the channels used as input. The results are saved in columns that have **channel names followed by "FJ"** (*DC2FJ, DC3FJ, FM0FJ-FM5FJ*). The FM*JF channels are evenly log spaced in energy.

Columns with **channel** names (like *E1*, *DC1*) describe the raw uncorrected count rate in 1/s measured by the channel. No corrections or cleaning were applied to these values. The use of the raw data is therefore at the risk of the user. The raw data can be the future basis for newly calibrated, independently corrected data sets that for example are less conservative of forcing potentially unreliable data to invalid values. However, such a data set should only be created by an experienced user familiar with all instrumental issues.

For data where the *HGA_Flag* column is 0, raw count rates were measured during steps 1-6 of the rotating platform (see Sec. 2.6). Count rates measured in step 0, behind the calibration shield, are provided in separate columns with **channel names ending with "BG"** (like *E1BG*, *DC1BG*). These rates are provided without any corrections applied to the data, so that they can directly compared to the other provided rates. The "BG" columns are only available in the low resolution file. In the case of times where the *HGA_Flag* column is 1, the data are not filtered for the calibration shield. Filtering needs to be done through the information provided in the *steps* column (Sec. 2.6).

After fractional year 1999.42 several channels were downlinked only in reduced resolution or not downlinked at all. This affects *As, EB2, FB1* that were not downlinked anymore, *F3, B0, B1, B2* that were degraded

from 6 to 1 sectors for *HGA_Flag*=0, and *TO3, TS2* that were degraded from 16 to 6 sectors. Raw data (entries in columns like *As, B1*) are to be considered wrong for these later times. We did not remove these wrong data because our philosophy here is to never change raw data. Calibrated data (like *B0J, B1I*) for these periods are corrected by providing interpolated values based on lower resolution measurements. *EB2, FB1* can be calculated with Eq. (6)-(7) but is not provided in the data files.

3.3.3 Auxiliary data

Times provided in the first columns mark the middle of the integration interval. Times are provided as fractional year in column **decyear**, as well as in the separate columns **Year, DOY, Hour, Min, Sec**. DOY is day of year, counted from day 1 on. When converting fractional year to DOY, ensure that round years (like 1995.00) are equal to DOY 1, not DOY 0. The provided fractional year values account for leap years but not leap seconds, meaning that fractional year values during 1995, 1997, and 1998 may be off by one second. Time tags are based on the aephdb.tfdos, aephdb.tfdos, atimeb.time_1, atimeb.time_6, and atimeb.time_16 variables found in the raw binary data files that are then interpolated to the provided resolution.

Other EPD data sets have shown time tags that at times differ by up to a spin period or integration interval, indicating that there may be an uncertainty regarding the absolute time tags in some of the existing data. Directional particle distributions on the other hand are usually consistent between different EPD data sets. We therefore suggest to always use the directional information provided within a given data set (such as this one) and not blindly combine different data sources (this one plus SPICE for example) based on a time tag.

Instrument look direction is provided relative to the magnetic field and Sun direction. Angles are provided in degrees. Pitch angle information is unreliable when HGA_Flag=0 (Sec. 5.3). **angle** is the angle relative to the Sun.

PAloc is the local pitch angle in degrees between the locally measured magnetic field and the local particle velocity vector, not the instrument look direction vector that would point exactly the opposite way. Many other EPD data sets, including the data previously published in the PDS and previous versions of our cleaned data set (until v26), were using the opposite definition despite claiming otherwise. PAloc covers values from $0°$ to $180°$.

PAeq is the equatorial pitch angle in degrees where we traced the particle to the magnetic equator using the Khurana field model (*Khurana and Schwarzl*, 2005; *Khurana et al.*, 2009) and calculated the angle between velocity and field there. PAeq covers values from $0°$ to $90°$ and therefore implies a trapped distribution. The used field model focuses on reproducing a large range of magnetospheric currents (more than some contemporary models such as *Connerney et al.* (2020)). Its internal field model is outdated (*Connerney et al.*, 2021), however that internal field becomes only critical near Jupiter's surface where Galileo took little data.

Bx, **By**, **Bz** are the measured magnetic field in nT in the Jupiter Solar Ecliptic (JSE) coordinate system. In the used system, x points toward the Sun, z toward ecliptic north, and y completes the right-handed system (*Lagg*, 1998). Note that other names exist for this system and that the abbreviation has been used for other systems (*Bagenal and Wilson*, 2016).

Bmodel is the local, total magnetic field in the Khurana field model (*Khurana et al.*, 2009) in nT.

Distances are provided in multiples of Jupiter's radius ($1R_J = 71492$km) - this is the standard equatorial radius used by SPICE. Galileo's position is provided here in the JSO coordinate system. JSO is sometimes also called JSE or GSE. The x axis points towards the Sun, z points roughly towards ecliptic north, and y completes the right-handed system (columns **gseX, gseY, gseZ** in R_J). For convenience we also provide the radial distance to Jupiter (**radialDist** in R_J), the azimuthal local time (**locT** in hours), the latitude relative to Jupiter's equatorial plane (**Lat3** in degrees), which is defined by its rotation axis. The local time is 12h for the location at local noon, between the planet and the Sun, and 0h for the location at local midnight, on the planet's nightside.

Galileo location is also provided relative to the magnetic field: Khurana L-shell (**LKhurana** dimensionless quantity of multiples of R_J), magnetic latitude (**latM** in degrees) relative to the Khurana current sheet, and the largest equatorial pitch angle that can reach the respective magnetic latitude of Galileo (**PAcut** in degrees, covers values from $0°$ to $90°$). The Khurana L-shell is the radial distance where the field line connected with the spacecraft passes the current sheet from the Khurana magnetic field model (*Khurana et al.*, 2009). Sometimes this quantity is called M-shell. The spacecraft distance normal to the Khurana plasma sheet can be calculated as $z_m = \mathrm{radialDist} \cdot \sin \mathrm{latM}$.

Galileo's longitude in the right-handed SIII system that rotates with the planet, also called east longitude, is provided in column *S3LonRH* in degrees.

Raw EPD measurements only provide differential electron intensities up to ≈700keV (F3 channel). At higher energies, measurements require further processing (Sec. 4.3). The result of this processing are spectral parameters that are valid from ≈700keV to ≈20MeV. The upper limit is because we are able to resolve spectral features up to this energy (Fig. 14, *Kollmann et al.* (2018)). These parameters are listed in columns **ParaG, ParaY**, and **ParaC**. They can be turned into intensities as follows

$$J = \frac{10^{ParaG*Log[W]+Log[ParaY]-2.60234*ParaG}}{1+e^{(W-10^{paraC})/(3\times10^3)}} \tag{3}$$

J is the differential intensity in 1/(cm^2 keV s sr). W is the energy in keV and can be chosen between ≈700keV to ≈20000keV. Results will be unreliable if energies outside this range are used. Intensity values at a few predefined W values are provided in columns with channel names followed by "f" (B1f, DC2f, DC3f).

3.4 CMS event data

There are two separate file types: **"cms_tof" file** for the EPD/CMS/TOFxE and **"cms_deltaexe" file** for the EPD/CMS/DeltaExE instruments. The EPD/CMS/TOFxE file combines data from HGA and LGA mode. EPD/CMS/DeltaExE is only available in HGA mode.

Times provided in the first two columns. The first column is called **Year.DOYHHMMSSM**. It is a string of the format: Year (4 digits) .(dot) day of year (3 digits) hour (2 digits) minutes (2 digits) seconds (2digits) tens of a second (1 digit). The second column is called **Decyear** and is the fractional year.

The columns **spin**, **step**, **HGA_flag** are the same as for the channelized data (Sec. 3.3.3).

The columns **Energy_keV**, **Ej_keV**, and **Ek_keV** show the deposited energy of the particle in keV. Energy deposition is in the respective solid state detectors KT, J, and K (see Fig. 1 for their location). Note that the deposited energy is lower than the ambient energy of the particle due to the pulse height defect and because the energy was reduced when the particle passed the START foil and detector dead layer.

The column **TOF_ns** lists the ion time of flight within the CMS/TOFxE instrument between the START foil and the KT detector. Combining energy and TOF measurement or two energy measurements allows determining the ion mass. Note that the ion in the instrument is slower than in ambient space because it lost energy when passing the START foil.

The column **detector** is 0 for TOFxE end, 1 for Jb/Kb and 3 for Ja/Ka of the two DeltaExE ends.

The column **etcode** includes information of unknown meaning that we still include for completeness.

4 Corrections to the data

This section documents how the provided intensity values were filtered and processed and discusses limitations of the data quality.

4.1 Dead time correction

A major issue of some of the Galileo/EPD/LEMMS data is that the instrument saturated when intensities became too high, which was usually the case close to Jupiter at $L < 30$. In these cases, the instrument provided high count rates that were only weakly dependent on the actual intensities. This behavior is illustrated in Fig. 11: While intensities commonly show variations over up to two orders of magnitude, most intensities near the planet are at a constant level.

Saturation of measured count rates occurs because a particle instrument is after the detection of one particle unable to count the next particle before the passage of the instrument's dead time T_D. For example, when the electronics behind a solid-state detector is processing a pulse associated with a particle it will not count another particle before being finished with processing. If N particles arrive during a time ΔT the rate $R_m = N/\Delta T$ measured by a saturating instrument is related to the actual rate R_a as (*Knoll*, 2000)

$$R_a = \frac{N}{\Delta T - N\,T_D} = \frac{R_m}{1 - T_D R_m} \tag{4}$$

This equation is exact for the rates of singles channels that count particles detected in a single SSD. It is approximately true for rates of channels using one detector with dead time T_D in anticoincidence with another detector (as it is the case for the E and F channels). For the channels that rely on the coincidence of two

detectors, we use the detector with the higher singles rate in the saturation region (B detector for B channels, D detector for DC channels). For F0 that accepts counts from two detectors, we use the F detector, since its saturation behaves similarly to F0.

If the instrument saturates, the count rate becomes

$$R_D = \frac{1}{T_D} \tag{5}$$

irrespective of the actual rate of particle arrival (see for example *Knoll* (2000), Sec. 4). Previous corrections to the LEMMS data mitigated the saturation by assuming dead times based on various calibration campaigns. However, this did not remove the shown behavior since the correction is very sensitive on the assumed value of the dead time. In order to improve upon this, we determined the dead time based on in-flight data by finding the maximum rate R_D of each SSD detector over the entire mission and used R_D and Eq. (5) to calculate the dead time.

The rates of the SSDs are called "singles" rates as no coincidence is involved. Downlinking the singles rates for detectors E and F was never planned and downlinking of channels As, EB2, and FB1 stopped in 1999. In order to perform the dead time correction and get R_D, we reconstructed the singles channels. The singles rate As of the A detector is just the sum of the coincidence channels:

$$As = A0 + A1 + A2 + A3 + A4 + A5 + A6 + A7 + A8 + B0 + B1 + B2 \tag{6}$$

The rates for the E1 and F1 detectors (note that these are different from the E1 and F1 channels) can be calculated similarly. The count rate of the F0 channel is split between detectors as it sums over counts from both detectors (Tab. 1).

$$Es = E0 + E1 + E2 + E3 + EB1 + EB2 + 0.5\ F0$$

$$Fs = F1 + F2 + F3 + FB1 + FB2 + 0.5\ F0$$

The FB and EB channels are designed to measure sideways penetrating particles. We estimate the rate of FB1 and EB2 based on the median ratio they had with their adjacent channel during times where all FB and EB channels were downlinked.

$$FB1 = 0.38888886\ FB2$$

$$EB2 = 1.1250003\ EB1 \tag{7}$$

For the detector F1 we find $R_D = 9 \times 10^5$/s, for the SSDs C, D, and E1, we find $R_D = 5 \times 10^5$/s, all reasonably consistent with nominal dead times of $T_D \approx 1\mu$s. The rates for the A and B detectors are lower and therefore do not seem to suffer from saturation. For completeness, we assume that their dead time is equal to the C, D, and E1 detectors. Based on the LEMMS analog processing (*Williams et al.* (1992), Fig 8), the dead time of F1 is not expected to be different to the other SSDs.

Sample data after applying Eq. (4) and the determined dead times are shown in Fig. 11. It can be seen that the dead time correction removes the saturation. The correction provides good estimates on the radial intensity distribution (Fig. 18A) since the uncertainty in the dead time correction is less than the L-dependence of the intensity. The procedure does not provide robust spectra around 130keV, which is the transition energy between two different SSDs used in LEMMS (E and F detectors) that have different dead times. Since the spectrum around 130keV is relatively flat, the results are sensitive to the dead time correction and even the corrected data cannot be used to reliably determine the spectral shape in this range. After applying the dead time correction, we therefore check if the corrected data show an intensity jump at energies transitioning between the E and F channels and remove the data from the E channel (that has a stronger correction) if that is the case. Also, to ensure that our analysis is not compromised by artifacts of the dead time correction, our forward model only relies on energies > 174keV (channels F1 and above).

4.2 Background and contamination

The difficulty in analyzing data from energetic particle instruments is that their channels sometimes count "out-of-passband" particles outside the nominal energy or mass range. This behavior is often called contamination with a background signal. In order to help mitigate this issue, EPD was mounted on a platform that repeatedly placed EPD behind a calibration shield (Sec. 2.6). This shield blocked the foreground intensities of particles that EPD was designed to measure.

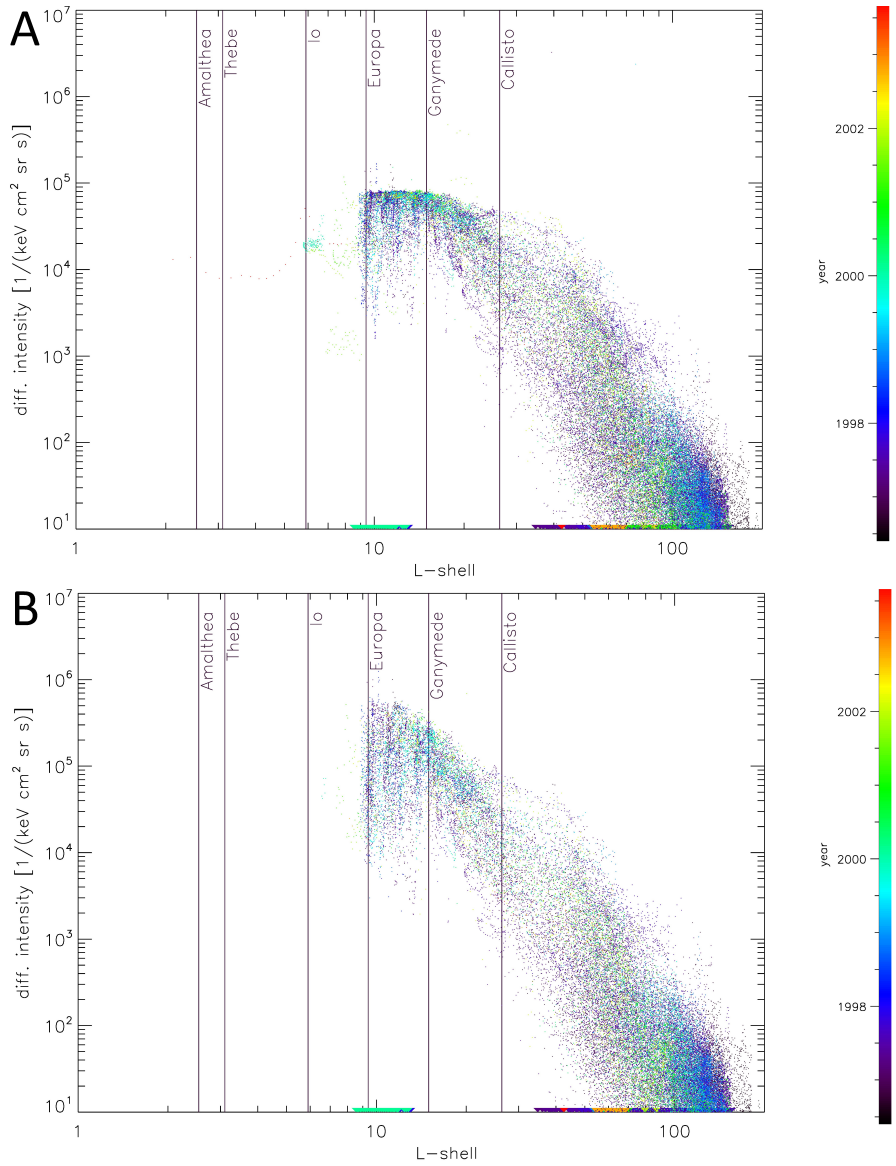

Figure 11: Intensity of 72keV electrons (E3 channel) throughout the mission before (panel A) and after (panel B) the corrections described in Sec. 4. Most significant is the dead time correction that lets the uncorrected intensities of this channel saturate at $\approx 10^5/(\mathrm{cm}^2$ keV sr s), while the actual intensities can at times be a factor of $\approx$ 10 larger. This effect is most significant for data from the E detector measuring $<$ 93keV electrons. The corrected data also removes most data of this energy inward of Europa's orbit since it is unreliable due to contamination. Some other channels provide reliable data up to smaller distances, see Fig. 18A.

LET data behind the calibration shield (motor step 0) is immediately available in the LGA-1 data that natively distinguishes step 0 and otherwise (see Fig. 9). For LGA-6 and LGA-16 we linearly interpolate the LGA-1 LET data behind the shield. During HGA mode we filter for LET measurements in motor step 0, which is when LET is behind the shield.

The HET does not fully go behind the calibration shield but shows large obscuration in step 5 (Fig. 4). To approximate background for the HET during HGA modes, we filter for step 5. We then bin the respective measurements over 3min, apply a median filter that removes the smallest 10% and largest 10% of the measurements, linearly average the remaining data, and linearly interpolate them between the center times of each bin. The interpolated background may appear to vary a lot for times or channels with low counting statistics. Unfortunately, step 5 is not resolved in the LGA measurements. This explains why HET channels in LGA mode show similar intensities for measurements that are supposedly shielded and unshielded, contrary to the same comparison in HGA mode.

Comparison between measurements behind and away from the shield allow to estimate the contribution of background contamination that can make the data unusable. (All measurements are dead time corrected (Sec. 4.1) before comparing shielded and unshielded count rates.) Times where this estimate are not available are set to their negative value to tag them as unreliable. Make sure to remove negative values appropriately before further analyzing the data. (A second reason for the negative values is measurements behind the shield being suspiciously large, as explained below.)

The instrument was usually showing nonzero rates even when blocking the foreground with the calibration shield. There are two reasons for this:

1) In a low-intensity environment counts measured in this orientation are mostly from a weak calibration source mounted in the shield (see the blue area in Fig. 12).

When Galileo is in a low intensity environment, meaning that the shielded rate is low and shielded counts $\gtrsim$ unshielded counts (blue area in Fig. 12), we leave both rates unchanged. The unshielded data can be used as is, the shielded data can in principle be used to track and correct for instrument efficiency degradation (Fig. 16) but this feature is currently not used (Sec. 4.6).

2) In the high-intensity region close to Jupiter, the counts behind the shield are mostly from penetrating radiation (see the red track in Fig. 12). Because these penetrators are also present while the instrument does not point toward the shield, we can use these counts to estimate the background contaminating the foreground.

When Galileo is in a high intensity environment, which we define as shielded counts $>$ threshold (dashed line in Fig. 12), we may subtract the shielded counts from the unshielded counts before converting to intensities. (The count rates that are provided are before that subtraction or any other correction.) In order to do that subtraction we need to interpolate the shielded counts, which means that we assume that the background contamination is isotropic and slowly changing. If shielded rates $>$ unshielded rates, intensities are set to invalid (-1.000000E+38).

If shielded rates $<$ unshielded rates, we provide background subtracted intensity values for the LET. However, the background subtraction does not work perfectly and the data quality becomes questionable when shielded/unshielded < 4. If this is the case, intensity values are multiplied by -1. (Unreliable values are therefore negative but not equal to the invalid value of -1.000000E+38.) We purposely do not remove the questionable measurements so that they are available for experienced users who may use the absolute value of all intensity values to get upper limit intensities. However, we strongly suggest that you only use the reliable positive values. In any case, it is important that negative values are not considered as such when calculating average values for example when binning in time or location.

We perform the described background subtraction for all HGA data and for LGA/LET data. Background subtraction is not possible for HET channels in HGA mode because no measure of the background is recorded (see above). We therefore do not subtract values here. Instead, we remove LGA/HET measurements at locations were mission-averaged HGA/HET shielded/unshielded < 1. This affects DC0 at $2 \geq L \geq 5.9$. We set these data negative where shielded/unshielded < 4. This affects all DC0 and DC1-DC3 at $L \lesssim 3$.

After background subtraction, we set LET intensities in step 0 as invalid, as they do not describe a foreground signal. We also remove LET intensities in step 7 for reasons unrelated to the calibration shield (Sec. 4.5). HET data close to the calibration shield suffers obscuration (Fig. 4). We therefore set all HET intensities with *steps* ≥ 4 as invalid and only provide their count rates.

Removing data based on the calibration shield measurements is not sufficient. Intensities inward of Io's orbit are currently not well know but there are indications that >MeV electrons reach their largest intensity of the magnetosphere (*de Soria-Santacruz et al.*, 2016; *Nénon et al.*, 2017) and that even GeV ions are present (*Kollmann et al.*, 2021; *Roussos*, 2022). Such particles are able to penetrate through instruments and cause

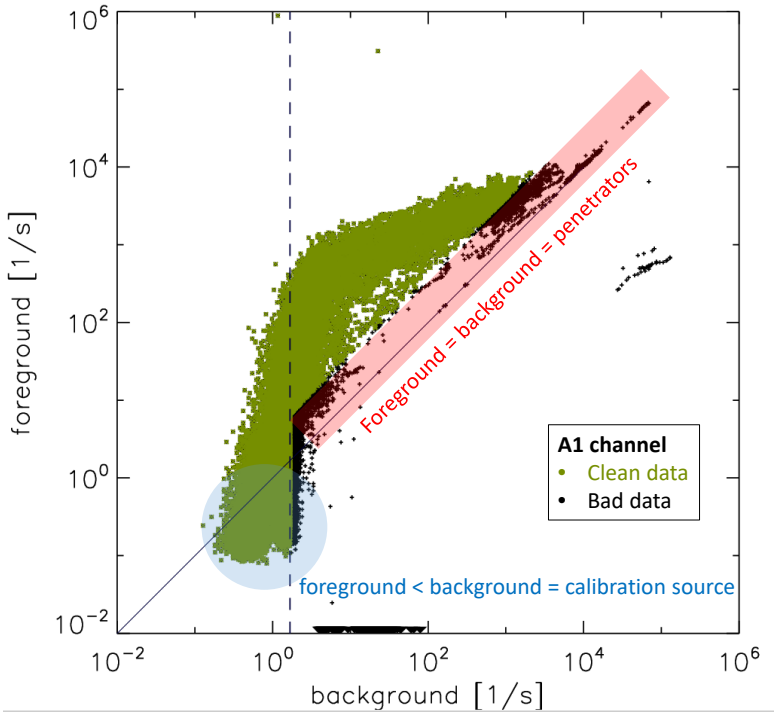

Figure 12: 38keV total ion (channel A1) count rate measured near-simultaneously in the magnetosphere, away from the calibration shield ("foreground" axis) and behind the calibration shield ("background" axis). Data points were accumulated throughout the mission. At times where foreground $\approx$ background (roughly the red area), the measurement is dominated by penetrating radiation, which is not useful and therefore removed from the calibrated data set. If foreground $>$ background, the foreground measurement can be used for science. Foreground $<$ background (roughly blue area) can happen if the magnetospheric count rates are smaller than the calibration source count rate (vertical dashed line). During such times, the foreground can be used to study the magnetosphere and the background can be used to measure the instrument response to the calibration source. Green points mark the foreground data that is usable. All other data is black.

wrong measurements in many EPD channels inward of Io. We therefore remove several channels detailed below for $L \leq 5.9$ that were not removed by the calibration shield method described above.

Channel B0 shows a relatively isotropic pitch angle distribution in this region. This suggests that particles penetrate the instrument from all sides, which is why the instrument direction does not organize the data anymore. We therefore remove this channel for $L \leq 5.9$.

While the A0-5 channels for HGA_Flag=0 are mostly removed based on the calibration shield inward of Io, their data persist for HGA_Flag=1. However, their measurements in that region are relatively isotropic and inconsistent with the relatively clean TP2 and TP3 channels. We therefore always remove these channels for $L \leq 5.9$.

B1 is relatively isotropic for $L \lesssim 3$ and shows a flat radial profile that suggests residual saturation. Integral intensity data was removed.

Event data reveal that also channels TP1, TO1, TO2 (and therefore also TOS1 and TOS2) are unreliable for $L < 5.9$ and that TH1 is always unreliable, see Fig. 13.

<MeV electron intensities measured with the E0-F0 channels at magnetic latitudes $\gtrsim 7°$ show a relatively steady decrease inward of Io. Spectra inward of Io at these latitudes however show a sharp increase for the F1-F3 channels, suggesting that they may be contaminated. It is commonly observed that contamination is a larger issue at lower magnetic latitudes (e.g. *Kollmann et al.* (2021)). Indeed we find that at $\lesssim 7°$ the combination of E and F channels shows unlikely spectra with several sudden jumps, suggesting that all involved channels are contaminated. Contaminated intensities are set to invalid.

There is no guarantee that all contaminated measurements were set to invalid. The user needs to keep in mind that surprising measurements sometimes can be an artifact of the measurement instead of a signature of an unexpected physical process. Contact the instrument team if in doubt.

4.3 High energy electron spectra

Channels providing differential intensities of electrons are only available for $<$ 0.7MeV (E and F channels). Above these energies, there are only channels providing integral intensities (B and DC channels). We determine differential intensities for $>$ 0.7MeV through a forward model. The forward model relies on the relation

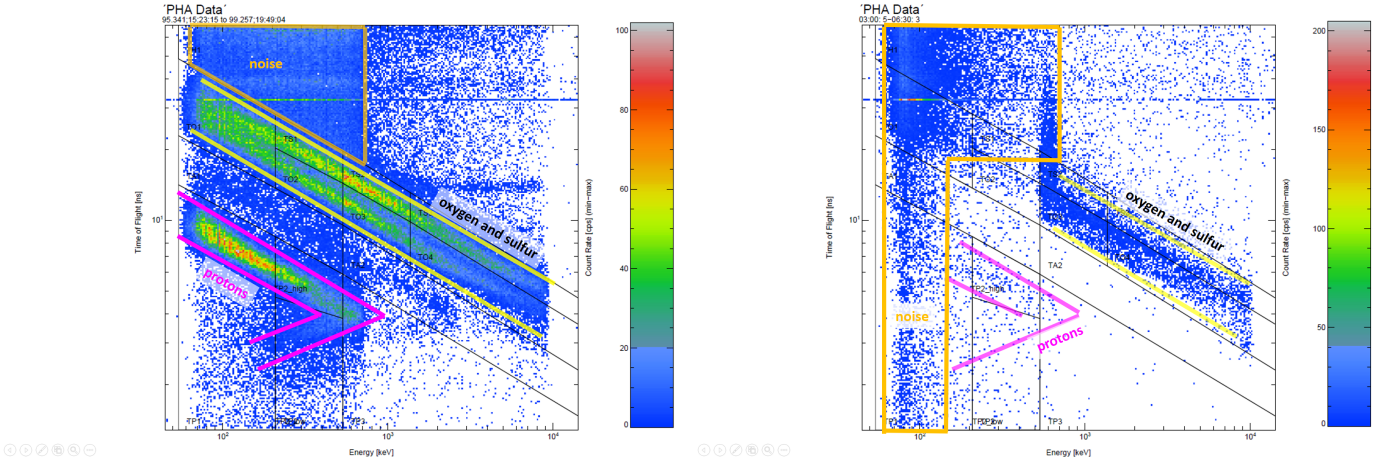

Figure 13: Event data of EPD/CMS/TOFxE (Sec. 2.7). Events from real ions form tracks following diagonal lines, everything else are instrumental artifacts that are caused for example by particles penetrating from the sides, causing arbitrary start, stop, and SSD signals. Black lines and labels like TP1 and TH1 mark the channel boundaries used to bin the measurements into channels (Sec. 2.3). Left: Long accumulation of event data in the early mission. Protons (pink outline) and oxygen and sulfur (yellow) form diagonal tracks at the expected locations. The area of the TH1 channel in the upper left corner is filled with false events, meaning that it counts noise, not real ions. Right: Event data during a short passage inward of Io's orbit (2002 DOY 309 3:00-6:30). It can be seen that there is a lot of noise in the low energy channels on the left (TP1, TO1, and TO2), which is why their intensities are removed in that region.

between count rate R_p (counted particles per time) and differential intensity j

$$R_p = \int_0^\infty \mathrm{d}E \; j(E) \; G(E) \tag{8}$$

G is the geometry factor of the instrument that can be considered as the instrument's effective area and solid angle. We use values from *Jun et al.* (2002) based on their Monte Carlo radiation transport simulations of the instrument. (Note that the publication by *Garrett et al.* (2012) shows the same values as *Jun et al.* (2002) in their Fig. 3 but listed outdated values in their Tab. 3.)

For the spectral shape we assume:

$$j = \left(\frac{E}{E_0}\right)^\gamma \frac{j_0}{1 + \exp\big((E - E_c)/K_T\big)} \tag{9}$$

Eq. (9) has the same energy dependence as Eq. (3). The intensity follows a power law with exponent $\gamma = paraG$ and cuts off at energy $E_c = 10^{paraC}$. $j_0 = paraY$ is the intensity at energy E_0. We select $E_0 = 400$keV (the center energy of channel F2). K_T determines how sharp the cutoff is. We fix it at $K_T = 3000$keV.

The overall intensity j_0 at E_0 and the exponent γ are determined by fitting j from the differential energy channels F1, F2, and F3 that cover 174-884keV (Tab. 1). We only keep fits where

$$\delta_k = |j_{f,k} - j_{m,k}|/j_{m,k} < 1 \tag{10}$$

The index k numbers the channels F1 to F3. $j_{m,k}$ is the measured differential intensity of the respective channel. $j_{f,k}$ is the respective fit value. The only free parameter remaining is the cutoff energy E_c.

We apply the forward model to the channels B1, DC2, and DC3. The implicit assumption here is that only electrons that enter through the instrument aperture are contributing to their count rates. Channel coincidences will reduce the contribution from electrons entering from the side. DC2 and DC3 also respond to high energy ($\gtrsim$ 20MeV) ions (*Jun et al.*, 2002). As the intensity at such high energies is low, we neglect their contribution.

Based on an initial guess of E_c, we calculate predicted rates R_p based on Eq. (8). These rates are then compared with the actually measured rates E_m of these channels. We quantify the total error as $\Delta = \sqrt{\sum_i (\log R_{p,i} - \log R_{m,i})^2}$. The index i numbers the channels B1 and DC2-DC3. Usually Δ is significant after the first iteration, so we change E_c until a match is found where Δ reaches a minimum. The change in parameters is done in an automatized way using the CONSTRAINED_MIN function available in the commercial

software Interactive Data Language (IDL) by Harris Geospatial Solutions, Inc. The error of each channel with running index i is quantified as

$$\delta_i = |R_{p,i} - R_{m,i}|/R_{m,i} \tag{11}$$

Even after a minimum is found, we only keep results with $\delta < 1$, equivalent to discrepancies less than a factor of 2. Around $L \approx 20$ 90% of the data has high enough quality to be fit and yields high-quality results. Outward from this distance the ratio drops, so that average intensities based on the forward model are not entirely representative.

Example spectra based on the forward model are shown in Fig. 20. We perform forward modeling throughout the entire mission and find cutoff energies up to tens of MeV (Fig. 14), indicating that the forward model works up to these energies.

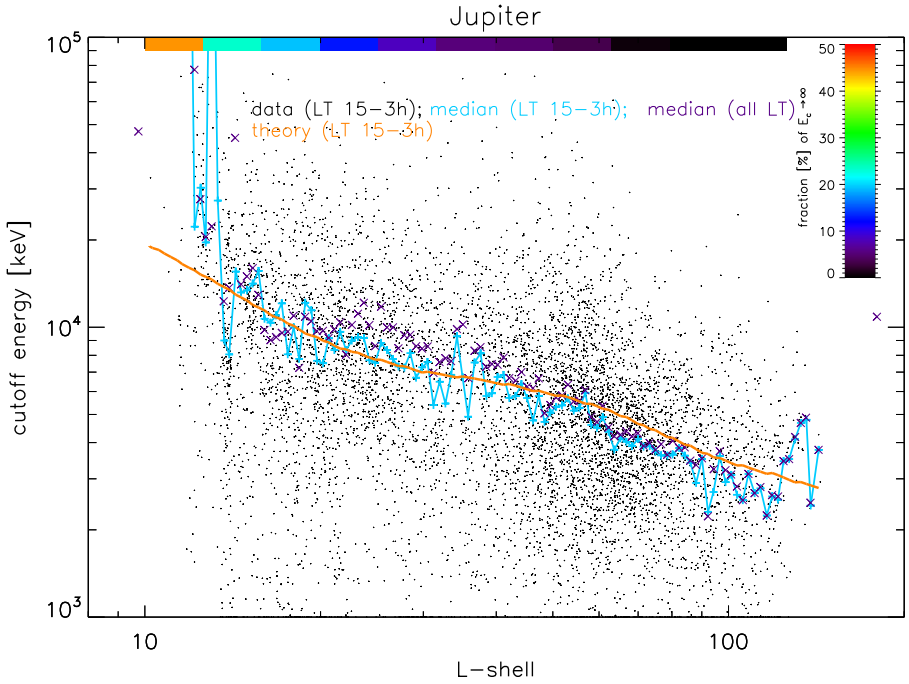

Figure 14: Cutoff energy E_c as a function of L-shell distance to Jupiter. Single points show all measurements throughout the missions. Their scatter illustrates that the shapes of the spectra are time variable. Data are limited to the evening side with local times in the range 15h-3h. The light blue curve and dark blue x-symbols show the median of the cutoff energies for the limited and full local time range, respectively. The orange curve compares these measurements with a theoretical expectation on how the cutoff would evolve based on radial transport and adiabatic heating (*Kollmann et al.*, 2018). If the cutoff energy is above tens of MeV, their precise value cannot be determined with the available data. We still keep track of the occurrence of such high cutoffs and find that they make up a significant fraction of the Jupiter fits for $L < 20$, which is illustrated by the color coding on top of the Jupiter panel.

4.4 Instrument degradation mitigation

Galileo and its instruments were subject to cumulative radiation damage in Jupiter's radiation belts that was affecting the instrument performance. This was mostly studied for the EPD/CMS/TOFxE instrument, as discussed here but may also affect the other instruments of the EPD package, as discussed in Sec. 4.6.

Radiation damage of a SSD builds up a dead layer over time in which particles are losing energy. Growth of the dead layer was gradual, so there is no hard boundary when it can be ignored. However, it but did not occur with the same speed and we consider it to be significant from 1999 on (e.g. *Lee-Payne et al.* (2020), their Fig. 3). The dead layer reached $0.3\mu m$ by 1999 and grew additional $0.05\mu m$ by the end of the mission (*Lee-Payne et al.* (2020), their Fig. 4).

In principle energy loss also happens in the active volume of a SSD but the loss in the dead layer is not measured. This means that over the course of the mission particles of the same energy deposit less and less energy in the active volume of the detector. This can be observed best in the event data (Sec. 2.7). The tracks of different ion species are shifting over time toward lower deposited energies (Fig. 15). The problem

is that the channel definitions still assume the original energy loss. This leads to the fact that sulfur events are split between the sulfur channels (TS1-TS3) and the oxygen channels (TO2-TO4), even though they should entirely reside in the sulfur channels. Count rates of these channels therefore cannot be immediately converted to intensities of oxygen and sulfur as it is the case in the early mission.

Because of this, we do not provide intensities of these channels from the beginning of 1999 on. Instead, we sum the count rates of oxygen and sulfur and create the artificial channels

$$TOS1 = TO1$$

$$TOS2 = TO2 + TS1$$

$$TOS3 = TO3 + TS2$$

$$TOS4 = TO4 + TS3$$

We provide differential intensities assuming that all counts in these channels were due to oxygen ions.

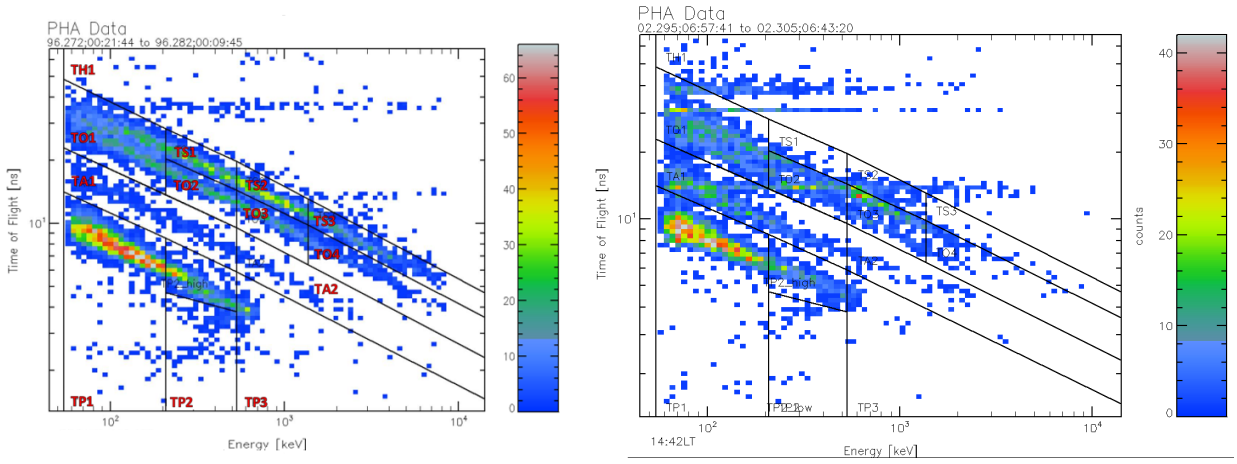

Figure 15: PHA event data from the EPD/CMS/TOFxE instrument. The x-axis shows the deposited energy of the recorded event, the y-axis the time of flight within the instrument. The number of events is binned in a 2D histogram and the color shows the number of events in each bin. Vertical and diagonal lines mark the boundaries of the CMS channels that are labeled with names like TP1 or TS3. Events forming tracks parallel to the diagonal lines are due to real ions. All other events are instrumental artifacts. Left: Undegraded measurements in 1996. It can be seen that the most events form tracks (red and green colors) within the channel boundaries. Right: Degraded measurements in 2002. It can be seen that the tracks shifted. This is most notably for the sulfur track (green diagonal near 600keV and 12ns), which is now split between the TO3 and TS2 channel boxes (black lines).

4.5 Anomalous instrument performance

There were several instances where EPD subsystems were not or are suspected to not perform nominally. During such periods we set calibrated data (in columns with channel names followed by a ”j”) to invalid.

Several reasons for anomalous performance were already discussed in Sec. 4.1-4.4. Another instance of anomalous performance is when the LET steps into motor position 7 (*Kollmann et al.*, 2016) in form of spikes and dips at least for CMS and the LEMMS A channels. It has been suggested that increased electronic noise the CMS START anode during that step that leads to increased measurements in TH and reduced measurements in the other channels (*Huybrighs et al.*, 2021).

4.6 Outstanding Issues

4.6.1 Unresolved instrument degradation

The channels for protons and alphas (TP and TA) do not have the problem that they are mixing particle species in the late mission as discussed in Sec. 4.4. However, the build up of the dead layer still means that particles with higher energies are required to trigger the channels toward the end of the mission. This is the reason why we provide different energy ranges after 1999 in Tab. 2. These energy values are not repeated in the data files.

Radiation damage has a further effect on the EPD/CMS/TOFxE instrument. Over time the efficiency of the microchannel plate (MCP) is decreasing, which reduces the efficiency to detect a particle. This is currently not corrected in the data.

Also the EPD/LEMMS instrument suffers degradation. We can observe this degradation using the onboard calibration alpha source. Fig. 16 shows count rates of the alpha calibration source measured with two A channels that respond to all ion species. These count rates were recorded during times where the calibration source yielded higher count rates than the space environment, measured by pointing the instrument away from the calibration source (blue area in Fig. 12). Most A channels change their count rates over the course of the mission, see the examples in Fig. 16. This effect is most notably in the A channels but relatively weak for the E and F channels. As the A channels are not that useful because they mix ion species (*Mauk et al.*, 2004), we do not correct for this effect in the provided data set.

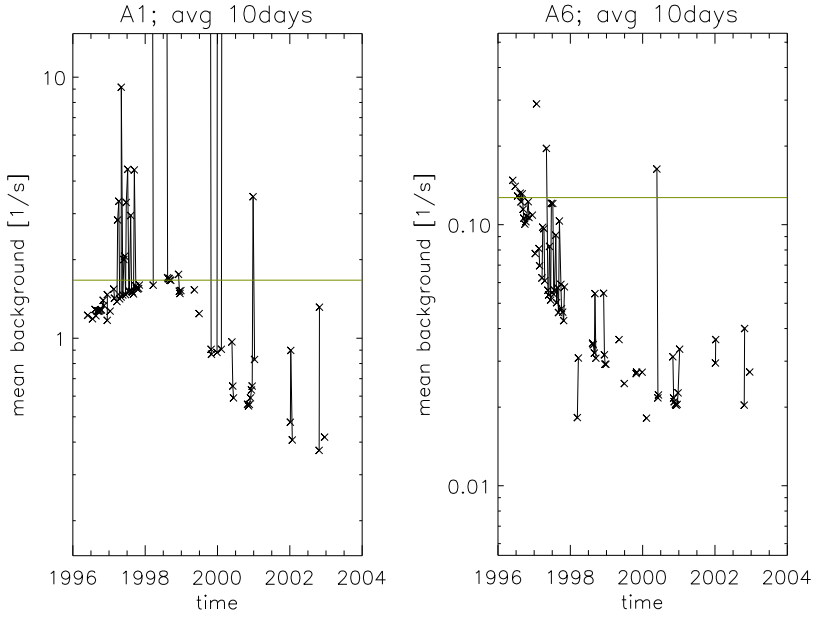

Figure 16: Count rates from the calibration source measured with two channels. It can be seen that the count rate decreases over time even though it should stay constant.

4.6.2 Mixed species channels

Some channels respond simultaneously to several particle species or different, non-consecutive energy ranges (Tab. 1-3). In principle, it is possible to disentangle the respective contributions with a technique similar as in Sec. 4.3. *Mauk et al.* (2004) disentangled ion species for a few periods where HGA data were available. No effort was made to apply such a technique to the whole data. For ions, this is not critical anymore because the recent Juno/JEDI instrument (*Mauk et al.*, 2013) is very well able to distinguish ion species with high energy and good mass resolution (*Haggerty et al.*, 2017). For electrons, clean data is already available outside of Io's orbit (Sec. 4.3). Inward of Io, more work is needed.

5 Example data

In this section we provide sample figures of the data and explain some possible pitfalls when using it.

5.1 Radial intensity profiles

Intensities can be displayed as a function of L-shell. Intensity values at the same L-shell show a large scatter (Fig. 17). This is not unusual, Saturn shares this behavior with Jupiter (*Kollmann et al.*, 2011). The scatter is in parts systematic, because the used L-shell is not the only relevant parameter, and in parts a result of true time dependence.

What we refer to in the text as the L-shell parameter and what is listed in the data files in the *LKhurana* column is the equatorial crossing point of a magnetic field line with the magnetic equator, calculated through the Khurana model. The main quantity that is important besides this parameter is the azimuthal location, described through the local time. The azimuthal location matters because the magnetosphere is not cylindrically symmetric: The dayside standoff distance of Jupiter's magnetopause is $60 - 110 R_J$ (*Krupp et al.*, 2004) while

the magnetotail extends over several AU (*Kurth et al.*, 1982; *Hill et al.*, 2009), well beyond Galileo's orbit. Systematic differences between particle intensities measured at different local times start to show at tens of R_J, depending on energy and species. At smaller distances, the magnetosphere is symmetric enough that different local times can be averaged together.

Other parameters that in principle may be important to organize the data are the pitch angle or equivalently, magnetic latitude. However, the pitch angle distributions measured by Galileo are all relatively flat (Fig. 22). This also means that the intensities reaching high latitudes are very similar to the intensities found in the equatorial plane. Filtering the data for pitch angle or latitude therefore does not significantly change the scatter and only reduces the number of used points.

Time variations yield much more significant fluctuations than pitch angle or latitude dependence. It is thought that most of the intensity variability over time arises from interchange injection events (Fig. 21, *Southwood and Kivelson* (1987); *Mauk et al.* (1999); *Paranicas et al.* (2016)).

Averaging over this variability is still instructive as it provides first insights into the physics governing the observed energetic particles (*Nénon et al.*, 2018) and because these averages can be used to design future spacecraft (*de Soria-Santacruz Pich et al.*, 2016). We show some example profiles of intensity as a function of L-shell in Fig. 18. Overall, all species increase toward the orbit of Io.

The occurrence at which different intensity values are observed does generally not follow a Gaussian distribution (Fig. 19), meaning that average value and standard deviation only provide a coarse description of the observed intensities. Particularly it should be noted that the median value is usually below the linear mean value, which is increased due to the long tail of high intensity values. The median is usually close to the peak of the intensity histogram, meaning that it is approximately the most likely intensity value to measure. The median is therefore a good quantity to design instrument performance to. The average value is for example useful to predict radiation damage.

5.2 Energy spectra

Energy spectra, both in the mission-average and instantaneous spectra, are to zeroth order power laws (Fig. 20).

Dynamics in the hundreds of keV range is in large part the result of injections (*Mauk et al.*, 1999) resulting from the interchange instability (*Southwood and Kivelson*, 1987). Such injections appear as sudden enhancements in particle intensity (see Fig. 21 green vs red below 100keV). A signature of injections vs. other mechanisms that can enhance intensities, like field-aligned beams (*Clark et al.*, 2018), is energy dispersion arising from the energy dependent gradient-curvature drift rates of energetic particles (*Burch et al.*, 2005; *Mauk et al.*, 2005). Dispersion means that the time of the intensity enhancement is different for each energy (green ledge). Such dispersion can lead to peaked energy spectra, where the location of the peak is time dependent (purple box).

5.3 Pitch angle distributions

Pitch angle distributions are nearly pancake (peaked near 90° and tapering off toward the field-line directions) in the inner magnetosphere but undergo a transition with radial distance to more field-aligned at larger Jovian distances (*Tomás et al.*, 2004a). However, all of these locally measured distributions are relatively flat and only change by a factor of a few over the full pitch angle range (Fig. 22, *Tomás et al.* (2004a); *Nénon and André* (2019)) when measured near Jupiter's equatorial plane. The latter is because the loss cone, near which intensities change a lot (*Mauk et al.*, 2016), is not resolved by measurements in the equatorial plane because it is much smaller than the opening angle of the instrument aperture. However, studies on details in the pitch angle distribution can reveal signatures of processes not accessible otherwise (*Tomás et al.*, 2004b; *Kollmann et al.*, 2016).

Long time averages usually average out pitch angle distributions. Averaging intensities at a certain location will blur out the pitch angle distribution even if a clear pitch angle dependence exists in each measurement. This applies even for averages in LGA mode with *HGA_Flag*=0. Measurements in this mode for example do not show the clear distribution shown in Fig. 22 at equivalent locations. Pitch angle information with *HGA_Flag*=0 should therefore be ignored unless confirmed to be reasonable, for example from comparison with equivalent *HGA_Flag*=1 data or physical expectation based on independent information.

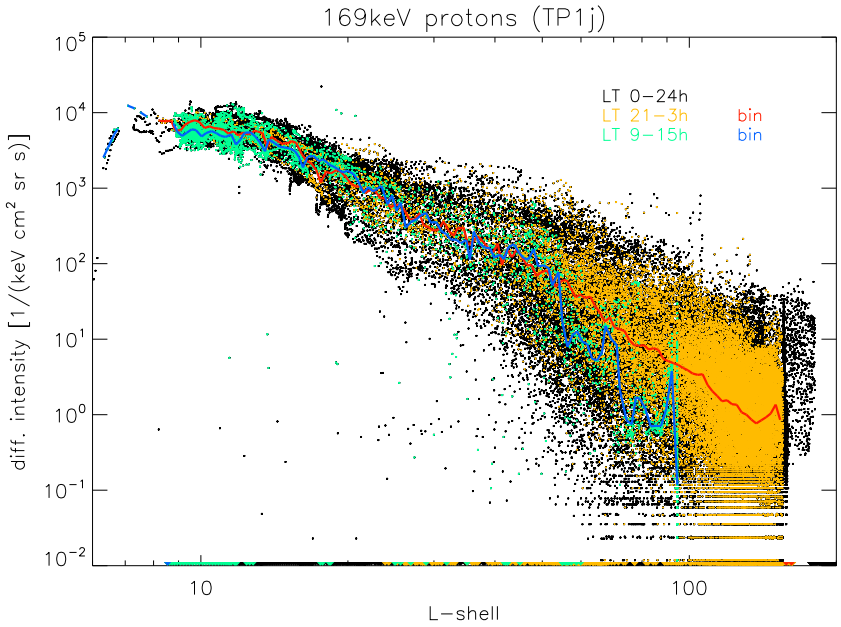

Figure 17: Intensities of 130-220keV protons (TP1 channel) as a function of L-shell. Black points: most data measured during the Galileo mission. Orange and green points: measurements filtered for the nightside and dayside of the planet, respectively. Red and blue curves: Linear average of the filtered data from the nightside and dayside. It can be seen that there is no systematic difference between the hemispheres close to the planet.

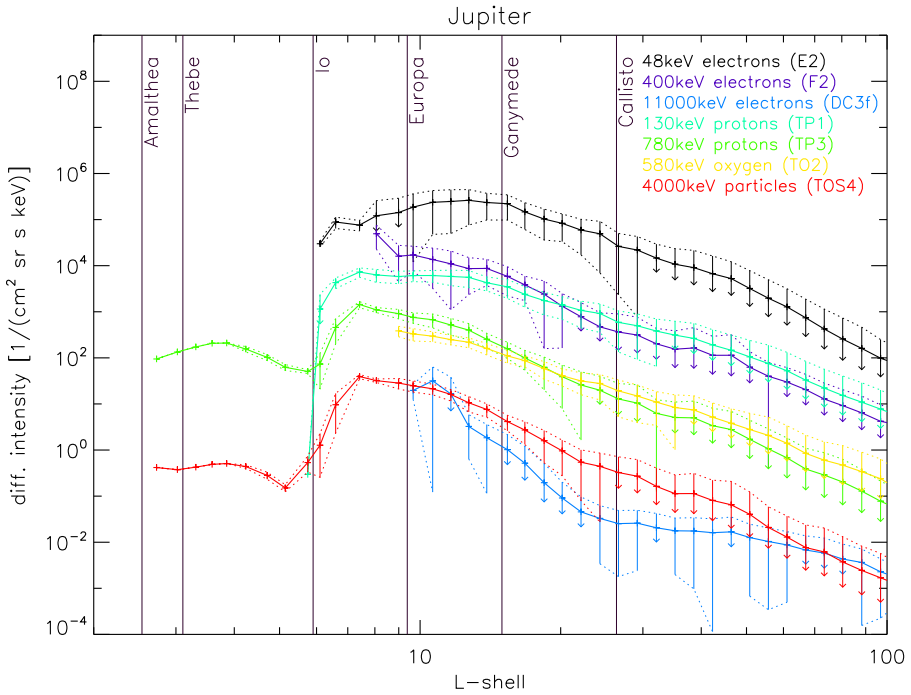

Figure 18: Intensities of various energetic particle populations as a function of L-shell. Measurements throughout the mission were cleaned from contamination (usually times of low intensities of the considered species and high intensities of penetrators), median filtered (removed the highest and lowest 1% of the data), and then linearly averaged. Error bars show the 1σ standard deviation, which indicates the time variability, not the Poisson uncertainty of the counts. Error bars ending in an arrow indicate that the error bar extends below the intensity range shown.

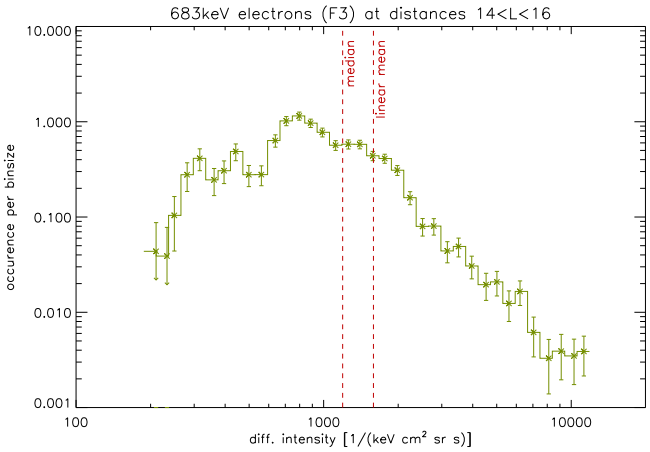

Figure 19: Intensity histogram of 527-884keV electrons (F3 channel) near the orbit of Ganymede. The histogram shows how often the intensity value on the horizontal axis is observed. Because the intensity bin that were used are log-spaced, we normalize the occurrence to the bin size to ensure a fair comparison.

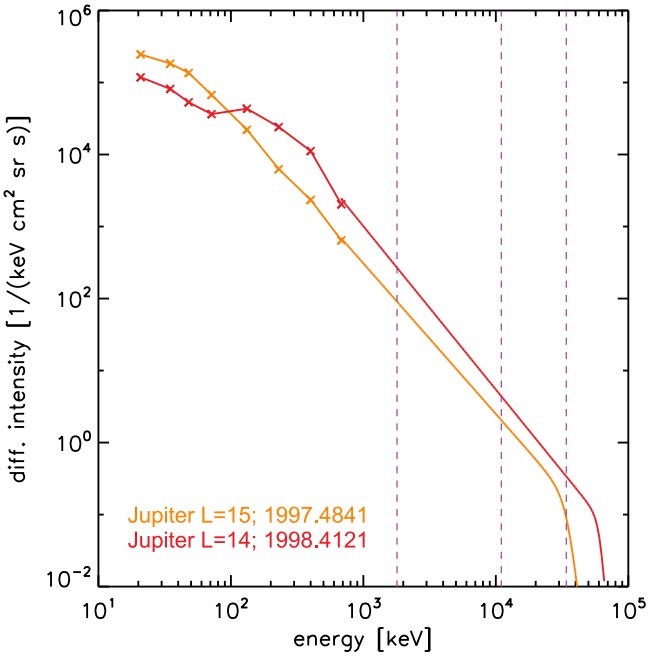

Figure 20: Typical electron spectra. The spectra are for $<$ 900keV based on differential intensity measurements. The center energies of the respective E and F channels are marked with "x"-symbols (*E0j* to *F3j* columns in the data file). At higher energies, spectra are based on a forward model (Sec. 4.3) and measurements by 3 integral energy channels (B1, DC2, and DC3). The energies above which these channels measure with more than 50% of their maximum efficiency are marked by vertical lines. The energies of highest efficiency are higher than these thresholds (up to 80MeV in the case of channel B1). Example intensities at high energies are provided in columns *DC2fj*, *DC3fj*, and *FM0-5fj* in the data file. There is variability in the electron spectra, some are smooth (orange curve, from 1997 DOY 177 17:06:54), others (red curve, from 1998 DOY 151 09:41:08) show for example signatures of dispersed injection events (*Mauk et al.*, 2005). Mission-averaged spectra (not shown) usually look smooth.

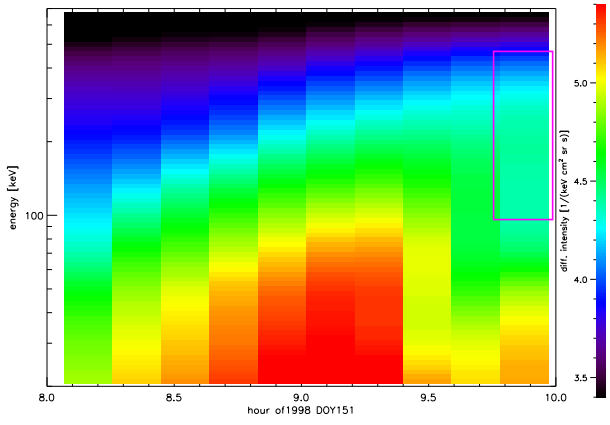

Figure 21: Example for an interchange injection in energetic electron data. For this plot, we interpolate the E and F channels to higher energy resolution. This trick makes it much easier to identify injections. (Comparisons with high resolution measurements are for example available for equivalent measurements at Saturn *Mauk et al.* (2005); *Paranicas et al.* (2016).) The purple box marks the peak in the red spectrum of Fig. 20.

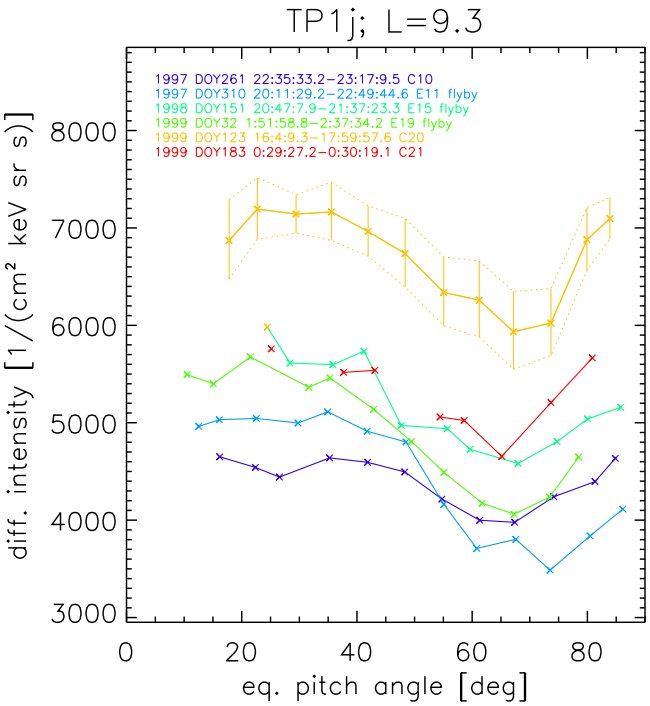

Figure 22: Equatorial pitch angle distribution of 130-220keV protons (*TP1j* column in the data files) near the L-shell (*LKhurana*) of Europa, measured in high time resolution (*HGA_Flag*=1). See *Kollmann et al.* (2016).

5.4 Event data

Every ”event” is the measurement of a single particle represented by a TOF and energy value (EPD/CMS/TOFxE), or two energy values (EPD/CMS/DeltaExE). Fig. 23 shows 2D histograms of events accumulated over several years.

It can be seen that events cluster in a way that forms tracks. Each track is for one ion species. For a TOFxE measurement, discrete tracks form because the relation between TOF (or actually velocity squared) and energy scales with the ion mass. As mass is an integer value, TOF(E) curves of different masses have gaps in between them. For a deltaExE measurement, species differ because the energy loss in the first solid state detector roughly scales with the square of the nuclear charge.

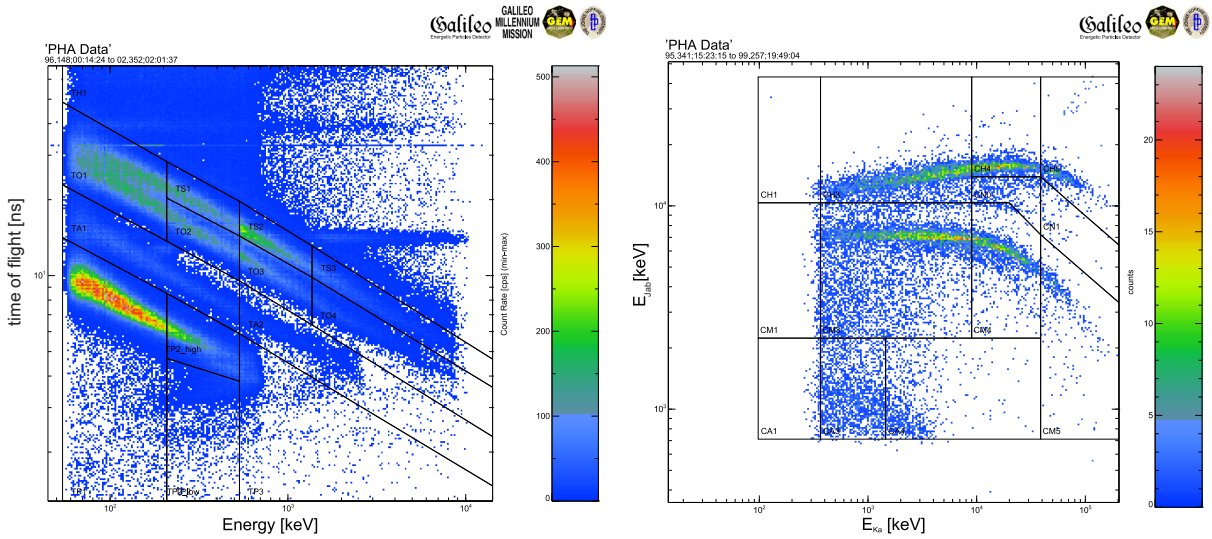

Figure 23: 2D histogram of event data that shows the number of events per bin in color. Left: data taken by the EPD/CMS/TOFxE instrument as a function of ion time of flight (TOF) and deposited energy in detector KT. Right: data by EPD/CMS/deltaExE, as a function of the deposited energies in detectors K and J. Black lines and labels indicate the boundaries of the rate channels. It can be seen that the event data provide much higher energy resolution.

6 Acknowledgements

This work was partly supported through NASA OPR and PDART grants NNX13AL06G and NNX15AN02G. We thank Quentin Nénon (University of California, Berkeley) and Hank Garrett (JPL) for reviewing parts of this manuscript. Thanks to everybody who was involved in building and maintaining Galileo and the EPD instrument.

References

Bagenal, F., and R. J. Wilson (2016), Jupiter Coordinate Systems, LASP Website, https://lasp.colorado.edu/home/mop/files/2015/02/CoOrd_systems12.pdf.

Becker, H. N., J. W. Alexander, A. Adriani, A. Mura, A. Cicchetti, R. Noschese, J. L. Jørgensen, T. Denver, J. Sushkova, A. Jørgensen, M. Benn, J. E. P. Connerney, S. J. Bolton, J. Allison, S. Watts, V. Adumitroaie, E. A. Manor-Chapman, I. J. Daubar, C. Lee, S. Kang, W. J. McAlpine, T. Di Iorio, C. Pasqui, A. Barbis, P. Lawton, L. Spalsbury, S. Loftin, and J. Sun (2017), The Juno Radiation Monitoring (RM) Investigation, *Space Sci. Rev.*, *213*, 507–545, doi:10.1007/s11214-017-0345-9.

Burch, J. L., J. Goldstein, T. W. Hill, D. T. Young, F. J. Crary, A. J. Coates, N. André, W. S. Kurth, and E. C. Sittler (2005), Properties of local plasma injections in Saturn's magnetosphere, *Geophys. Res. Lett.*, *32*, 14, doi:10.1029/2005GL022611.

Carlton, A., M. de Soria-Santacruz Pich, I. Jun, W. Kim, and K. Cahoy (2016), Using the Galileo Solid State Imager as a Sensor of Jovian Energetic Electrons, in *AGU Fall Meeting Abstracts*, pp. SM51A–2463.

Clark, G., C. Tao, B. H. Mauk, J. Nichols, J. Saur, E. J. Bunce, F. Allegrini, R. Gladstone, F. Bagenal, S. Bolton, B. Bonfond, J. Connerney, R. W. Ebert, D. J. Gershman, D. Haggerty, T. Kimura, P. Kollmann, S. Kotsiaros, W. S. Kurth, S. Levin, D. J. McComas, G. Murakami, C. Paranicas, A. Rymer, and P. Valek (2018), Precipitating electron energy flux and characteristic energies in jupiter's main auroral region as measured by juno/jedi, *J. Geophys. Res.: Space Physics*, *0*(0), doi:10.1029/2018JA025639.

Connerney, J. E. P., S. Timmins, M. Herceg, and J. L. Joergensen (2020), A Jovian Magnetodisc Model for the Juno Era, *Journal of Geophysical Research (Space Physics)*, *125*(10), e28138, doi:10.1029/2020JA028138.

Connerney, J. E. P., S. Timmins, R. J. Oliversen, J. R. Espley, J. L. Joergensen, S. Kotsiaros, P. S. Joergensen, J. M. G. Merayo, M. Herceg, J. Bloxham, K. M. Moore, A. Mura, A. Moirano, S. J. Bolton, and S. M. Levin (2021), A new model of jupiter's magnetic field at the completion of juno's prime mission, *Journal of Geophysical Research: Planets*, *n/a*(n/a), e2021JE007,055, doi:https://doi.org/10.1029/2021JE007055, e2021JE007055 2021JE007055.

Davis, M. W., G. T. G., C. M. Cooke, R. C. Blase, R. G. Gladstone, and K. D. Retherford (2016), Mev-level electron and gamma ray sensitivites of modern far ultraviolet sensitive microchannel plate detectors, doi:10.1117/12.2232755.

de Soria-Santacruz, M., H. B. Garrett, R. W. Evans, I. Jun, W. Kim, C. Paranicas, and A. Drozdov (2016), An empirical model of the high-energy electron environment at Jupiter, *J. Geophys. Res.*, *121*, 9732–9743, doi:10.1002/2016JA023059.

de Soria-Santacruz Pich, M., H. B. Garrett, R. W. Evans, I. Jun, W. Kim, and C. Paranicas (2016), The gire2 model and its application to the europa mission, in *2016 IEEE Aerospace Conference*, pp. 1–7, doi:10.1109/AERO.2016.7500516.

Garrett, H. B., M. Kokorowski, I. Jun, and R. Evans (2012), Galileo Interim Radiation Electron Model Update - 2012, JPL Publication 12-9, http://hdl.handle.net/2014/42026.

Haggerty, D. K., B. H. Mauk, C. P. Paranicas, G. Clark, P. Kollmann, A. M. Rymer, S. J. Bolton, J. E. P. Connerney, and S. M. Levin (2017), Juno/JEDI observations of 0.01 to >10 MeV energetic ions in the Jovian auroral regions: Anticipating a source for polar X-ray emission, *Geophys. Res. Lett.*, *44*(13), 6476–6482, doi:10.1002/2017GL072866.

Hill, M. E., D. K. Haggerty, R. L. McNutt, and C. P. Paranicas (2009), Energetic particle evidence for magnetic filaments in Jupiter's magnetotail, *J. Geophys. Res.*, *114*(A13), A11201, doi:10.1029/2009JA014374.

Hunt-Ward, T., and T. P. Armstrong (2003), Galileo EPD Handbook, Website, http://galileo.ftecs.com/.

Huybrighs, H. L. F., E. Roussos, A. Blöcker, N. Krupp, Y. Futaana, S. Barabash, L. Z. Hadid, M. K. G. Holmberg, and O. Witasse (2021), Reply to Comment on "An Active Plume Eruption on Europa During Galileo Flyby E26 as Indicated by Energetic Proton Depletions", *Geophys. Res. Lett.*, *48*(18), e95240, doi:10.1029/2021GL095240.

Jaskulek, S., and C. Crane (1993), New EPD Format and Implementation, Website, http://galileo.ftecs.com/Handbook/Chapter%202/new-epd-format.html.

Joy, S. (2009), Galileo Orbiter at Jupiter: EPD Scan Averages Data, Website, doi:\url{https://doi.org/10.17189/1519661}, https://pds-ppi.igpp.ucla.edu/ditdos/viewFile?id=pds://PPI/GO-J-EPD-2-REDR-RTS-SCAN-AVG-V1.0/AAREADME.TXT.

Jun, I., J. M. Ratliff, H. B. Garrett, and R. W. McEntire (2002), Monte Carlo simulations of the Galileo energetic particle detector, *Nuclear Instruments and Methods in Physics Research A*, *490*, 465–475, doi:10.1016/S0168-9002(02)01072-0.

Khurana, K. K., and H. K. Schwarzl (2005), Global structure of Jupiter's magnetospheric current sheet, *J. Geophys. Res.*, *110*(A9), A07227, doi:10.1029/2004JA010757.

Khurana, K. K., A. Shinn, M. Desroche, and R. Wilson (2009), Magnetic field model for Jupiter, available online, http://lasp.colorado.edu/home/mop/resources/graphics/code.

Knoll, G. F. (2000), *Radiation detection and measurement*, 3rd ed., John Wiley & Sons, New York, USA.

Kollmann, P., and T. H. Choo (2019), GALILEO Energetic Particles Detector (EPD) Homepage, Website, http://sd-www.jhuapl.edu/Galileo_EPD/.

Kollmann, P., E. Roussos, C. Paranicas, N. Krupp, C. M. Jackman, E. Kirsch, and K.-H. Glassmeier (2011), Energetic particle phase space densities at Saturn: Cassini observations and interpretations, *J. Geophys. Res.*, *116*(A15), A05,222, doi:10.1029/2010JA016221.

Kollmann, P., C. Paranicas, G. Clark, E. Roussos, A. Lagg, and N. Krupp (2016), The vertical thickness of Jupiter's Europa gas torus from charged particle measurements, *Geophys. Res. Lett.*, *43*, 9425–9433, doi:10.1002/2016GL070326.

Kollmann, P., E. Roussos, C. Paranicas, E. E. Woodfield, B. H. Mauk, G. Clark, D. C. Smith, and J. Vandegriff (2018), Electron acceleration to MeV energies at Jupiter and Saturn, *J. Geophys. Res.*, *123*(11), 9110–9129, doi:10.1029/2018JA025639.

Kollmann, P., G. Clark, C. Paranicas, B. Mauk, E. Roussos, Q. Nénon, H. B. Garrett, A. Sicard, D. Haggerty, and A. Rymer (2021), Jupiter's ion radiation belts inward of europa's orbit, *Journal of Geophysical Research: Space Physics*, *126*(4), e2020JA028,925, doi:https://doi.org/10.1029/2020JA028925, e2020JA028925 2020JA028925.

Krupp, N., V. M. Vasyliunas, J. Woch, A. Lagg, K. K. Khurana, M. G. Kivelson, B. H. Mauk, E. C. Roelof, D. J. Williams, S. M. Krimigis, W. S. Kurth, L. A. Frank, and W. R. Paterson (2004), Dynamics of the Jovian magnetosphere, in *Jupiter. The Planet, Satellites and Magnetosphere*, edited by Bagenal, F., Dowling, T. E., & McKinnon, W. B., pp. 593–616, Cambridge University Press, Cambridge, U.K.

Kurth, W. S., D. A. Gurnett, J. D. Sullivan, H. S. Bridge, F. L. Scarf, and E. C. Sittler, Jr. (1982), Observations of Jupiter's distant magnetotail and wake, *J. Geophys. Res.*, *87*, 10,373–10,383, doi:10.1029/JA087iA12p10373.

Lagg, A. (1998), Energiereiche Teilchen in der inneren Jupitermagnetosphäre: Simulation und Ergebnisse des EPD-Experimentes an Bord der Raumsonde GALILEO, Ph.D. thesis, Leopold-Franzens-Universität Innsbruck, Innsbruck, Austria.

Lagg, A. (2004), Galileo EPD Data Processing Software, IDL software http://www2.mps.mpg.de/homes/lagg/.

Lee-Payne, Z., P. Kollmann, M. Grande, and T. Knight (2020), Correction of Galileo Energetic Particle Detector, Composition Measurement System High Rate Data: Semiconductor Dead Layer Correction, *Space Sci. Rev.*, *216*(1), 5, doi:10.1007/s11214-019-0621-y.

Martinez Sierra, L. M., H. B. Garret, and I. Jun (2015), Radiation environment model of protons and heavier ions at jupiter, in *AIAA SPACE 2015 Conference and Exposition*, p. 4557, doi:10.2514/6.2015-4557.

Mauk, B. H., D. J. Williams, R. W. McEntire, K. K. Khurana, and J. G. Roederer (1999), Storm-like dynamics of Jupiter's inner and middle magnetosphere, *J. Geophys. Res.*, *104*, 22,759–22,778, doi:10.1029/1999JA900097.

Mauk, B. H., D. G. Mitchell, R. W. McEntire, C. P. Paranicas, E. C. Roelof, D. J. Williams, S. M. Krimigis, and A. Lagg (2004), Energetic ion characteristics and neutral gas interactions in Jupiter's magnetosphere, *J. Geophys. Res.*, *109*(A18), A09S12, doi:10.1029/2003JA010270.

Mauk, B. H., J. Saur, D. G. Mitchell, E. C. Roelof, P. C. Brandt, T. P. Armstrong, D. C. Hamilton, S. M. Krimigis, N. Krupp, S. A. Livi, J. W. Manweiler, and C. P. Paranicas (2005), Energetic particle injections in Saturn's magnetosphere, *Geophys. Res. Lett.*, *32*, 14, doi:10.1029/2005GL022485.

Mauk, B. H., D. K. Haggerty, S. E. Jaskulek, C. E. Schlemm, L. E. Brown, S. A. Cooper, R. S. Gurnee, C. M. Hammock, J. R. Hayes, G. C. Ho, J. C. Hutcheson, A. D. Jacques, S. Kerem, C. K. Kim, D. G. Mitchell,

K. S. Nelson, C. P. Paranicas, N. Paschalidis, E. Rossano, and M. R. Stokes (2013), The Jupiter Energetic Particle Detector Instrument (JEDI) Investigation for the Juno Mission, *Space Sci. Rev.*, doi:10.1007/s11214-013-0025-3.

Mauk, B. H., D. K. Haggerty, C. P. Paranicas, G. Clark, P. Kollmann, A. M. Rymer, L. E. Brown, S. E. Jaskulek, C. E. Schlemm, C. K. Kim, A. Adriani, S. J. Bolton, F. Bagenal, J. E. P. Connerney, G. R. Gladstone, W. S. Kurth, S. M. Levin, D. J. McComas, and V. P. (2016), Juno observations of energetic charged particles over Jupiter's polar regions: Analysis of mono-and bi-directional electron beams, *Geophys. Res. Lett.*, *accepted*, doi:10.1002/2016GL072286.

Nénon, Q., A. Sicard, and S. Bourdarie (2017), A new physical model of the electron radiation belts of Jupiter inside Europa's orbit, *J. Geophys. Res.*, *122*, 5148–5167, doi:10.1002/2017JA023893.

Nénon, Q., A. Sicard, P. Kollmann, H. B. Garrett, S. P. A. Sauer, and C. Paranicas (2018), A Physical Model of the Proton Radiation Belts of Jupiter inside Europa's Orbit, *J. Geophys. Res.*, *123*, 3512–3532, doi:10.1029/2018JA025216.

Nénon, Q., and N. André (2019), Evidence of europa neutral gas torii from energetic sulfur ion measurements, *Geophysical Research Letters*, doi:10.1029/2019GL082200.

Paranicas, C., M. F. Thomsen, N. Achilleos, M. Andriopoulou, S. V. Badman, G. Hospodarsky, C. M. Jackman, X. Jia, T. Kennelly, K. Khurana, P. Kollmann, N. Krupp, P. Louarn, E. Roussos, and N. Sergis (2016), Effects of radial motion on interchange injections at Saturn, *Icarus*, *264*, 342–351, doi:10.1016/j.icarus.2015.10.002.

Roussos, E. (2022), A source of very energetic oxygen located in Jupiter's inner radiation belts, *Science Advances*.

Selesnick, R. S., and J. B. Blake (2000), On the source location of radiation belt relativistic electrons, *J. Geophys. Res.*, *105*, 2607–2624, doi:10.1029/1999JA900445.

Southwood, D. J., and M. G. Kivelson (1987), Magnetospheric interchange instability, *J. Geophys. Res.*, *92*, 109–116, doi:10.1029/JA092iA01p00109.

Tomás, A., J. Woch, N. Krupp, A. Lagg, K.-H. Glassmeier, M. K. Dougherty, and P. G. Hanlon (2004a), Changes of the energetic particles characteristics in the inner part of the Jovian magnetosphere: a topological study, *Planet. Space Sci.*, *52*, 491–498, doi:10.1016/j.pss.2003.06.011.

Tomás, A. T., J. Woch, N. Krupp, A. Lagg, K.-H. Glassmeier, and W. S. Kurth (2004b), Energetic electrons in the inner part of the Jovian magnetosphere and their relation to auroral emissions, *J. Geophys. Res.*, *109*, A06203, doi:10.1029/2004JA010405.

Williams, D. J., R. W. McEntire, S. Jaskulek, and B. Wilken (1992), The Galileo Energetic Particles Detector, *Space Sci. Rev.*, *60*, 385–412, doi:10.1007/BF00216863.